photonics

MDPI

Article

A Pole-Based Approach to Composite Linear Optical Cavities with Internal Dielectric Reflectors

Vedran Vujnović [1,2], Nenad Kralj [2,*] and Marin Karuza [2,3]

[1] Medical Physics and Radiation Protection Department, University Hospital Rijeka, 51000 Rijeka, Croatia
[2] Faculty of Physics and Center for Micro- and Nanosciences and Technologies, University of Rijeka, Radmile Matejčić 2, 51000 Rijeka, Croatia
[3] Istituto Nazionale di Fisica Nucleare, Sezione di Trieste, Via Valerio 2, 34127 Trieste, Italy
* Correspondence: nenad.kralj@phy.uniri.hr

Abstract

We develop a versatile description of Fabry–Pérot resonators comprising internal dielectric structures, based on transfer matrices and interpreted from a non-Hermitian one-pole self-energy viewpoint. For a two-mirror cavity containing an internal slab of arbitrary thickness and refractive index, we derive closed-form expressions for transmission and identify cavity poles as zeros of the reduced denominator in the complex-frequency plane. For a weak-reflector, we obtain leading-order expressions for the pole shifts of individual modes and show that the resulting mode pulling and linewidth change are, respectively, governed by the imaginary and real parts of a single complex quantity formed by the coherent sum of two mirror-side scattering paths. These expressions provide placement criteria for dispersive or dissipative operation and support practical workflows for extracting weak-reflector parameters from measured resonance traces, predicting slab-modified cavity spectra from the empty cavity calibration, and designing doubly resonant cavities with fine constraints on slab position. We extend the consideration to multiple reflectors, with emphasis on two-membrane and three-mirror geometries, relevant to coupled filter cavities and membrane-in-the-middle architectures. The coupled-pole parametrization relates these configurations, providing a compact framework for the analysis and design of composite Fabry–Pérot elements for precision filtering and quantum-noise shaping in advanced interferometric experiments.

Keywords: Fabry–Pérot cavity; transfer-matrix; complex frequency response; three-mirror cavity; cavity optomechanics; optical self-energy; membrane-in-the-middle

1. Introduction

Fabry–Pérot (FP) resonators containing partially reflecting internal elements appear in a variety of optical systems, ranging from internal etalons and compound FP filters for mode shaping, tunable filtering, and intracavity spectroscopy [1–6], across three-mirror [7] and grating-coupled [8] cavities for improved control and power recycling in gravitational-wave detectors, to membrane-in-the-middle setups [9,10] establishing a distinct experimental branch of cavity optomechanics [11]. In all of these settings, the internal element reshapes the resonance spectrum of the bare cavity: longitudinal modes are shifted in frequency and modified in linewidth, while multiple internal reflectors generate coupled-resonance structures that can be exploited for filtering and response engineering [6–8]. This broader intracavity-resonator landscape also includes cavity-enhanced spectroscopy and sensing

Check for updates

Received: 11 July 2026
Revised: 24 July 2026
Accepted: 27 July 2026
Published: 30 July 2026

Copyright: © 2026 by the authors. Licensee MDPI, Basel, Switzerland. This article is an open access article distributed under the terms and conditions of the Creative Commons Attribution (CC BY) license.

platforms, where internal or intracavity resonant elements are used to increase interaction length and spectral selectivity [3,4,12].

For thin, weakly reflecting membranes, studies of cavity optomechanics often present the eigenfrequencies in a compact non-perturbative form with a well-known arccosine dependence on membrane position [9,11]. Related scattering-based treatments also show that once one moves away from the standard MIM geometry, the position dependence of the resonance frequencies need not follow the arccosine form [13]. These formulations make the periodicity and dispersive tuning apparent, but they do not explicitly show how the full complex resonance shift separates into frequency and linewidth corrections and are not readily generalized to thick, absorptive internal slabs. In practice, cavities containing thick internal slabs, absorptive internal elements, or multiple internal reflectors are typically treated either numerically or with ad hoc approximations that obscure the underlying pole structure and its dependence on design parameters. Examples include three-mirror and coupled-cavity systems treated primarily with transfer-matrix or related input–output formalisms [7,8,14], as well as two- and multi-membrane cavity systems analyzed mainly through matrix-based frequency calculations rather than explicit analytic pole tracking [15–18]. Even in canonical treatments of MIM, analytic expressions beyond the thin-membrane limit are typically approximate and do not yield explicit pole trajectories. Interferometer studies involving etalon substrates, thermal lensing, and intra-cavity compensation plates are likewise often treated with dedicated numerical optical models or experiment-specific simulations, rather than with explicit analytic pole-tracking formulae [19–21].

The aim of our work is to provide a unified and practical pole-based treatment of FP cavities containing internal dielectric elements. Compared to conventional transfer-matrix treatments, which primarily provide the full frequency-domain response, and coupled-cavity models, which rely on a chosen reduced-mode parametrization, the present approach derives an analytic pole-level reduction directly from the exact slab transfer-matrix. For a two-mirror cavity containing a single internal slab, we formulate a closed-form reduced-denominator description and show how its weak-reflector limit admits a non-Hermitian one-pole Green-function/self-energy interpretation, while keeping the final results in a mode-resolved form suited to analysis and experiment. Specifically, in the weak-reflector regime, the cavity linewidth and resonance frequency change are governed by the real and imaginary parts of a single complex quantity. This allows for a concise and elegant representation from which the magnitude of both changes can easily be quantified as a certain parameter, e.g., slab position, is swept. Alternatively, the value of this tunable or fluctuating parameter can be estimated from the model if the cavity parameters are independently measured. The identification of slab positions for predominantly dispersive or dissipative operating points is thus also facilitated. As an example, we describe finding positions suitable for a two-wavelength scheme used to ascertain the object's presence inside the cavity while aiming to avoid absorption. Beyond the single-slab case, we extend the pole-based treatment to multiple internal reflectors, obtaining a compact parametrization that connects single-slab, two-reflector, and three-mirror geometries and is relevant to composite FP design for filtering and quantum-noise shaping in advanced interferometric systems [22–26].

The paper is organized as follows. Section 2 introduces the cavity geometry, notation, and transfer-matrix framework. Section 3 derives the exact single-slab transfer function and pole condition. Section 4 develops the weak-reflector asymptotics and practical design and calibration workflows. Section 5 extends the formalism to multiple internal reflectors and illustrates direct pole tracking under parameter sweeps. Section 6 summarizes the main results and discusses future research directions.

2. Model and Notation: Cavity Geometry and Transfer Matrices

We consider an FP cavity of total length L bounded by two end mirrors, M_1 and M_3 on the input and output sides, respectively (see Figure 1). The mirrors are characterized by complex amplitude reflection and transmission coefficients (r_1, t_1) and (r_3, t_3). Throughout, we assume normal incidence and adopt the time dependence $\exp(-i\omega t)$ for the fields. The complex resonance frequency of a given composite cavity mode μ is denoted by $\tilde{\omega}_\mu \in \mathbb{C}$, where $\omega_\mu \equiv \mathfrak{Re}\,\tilde{\omega}_\mu$ represents the resonance frequency, while the linewidth is defined as $\kappa_\mu \equiv -2\,\mathfrak{Im}\,\tilde{\omega}_\mu > 0$. The symbol r_m shown in Figure 1 is not an independent slab parameter; it is introduced later as an effective weak-reflector quantity derived from the slab response.

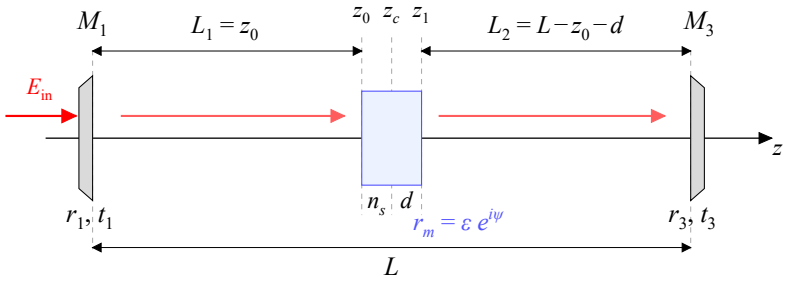


Figure 1. Fabry–Pérot cavity of length L with end mirrors M_1 and M_3 and an internal slab (index n_s, thickness d) centered at z_c (front face at z_0). The slab is treated exactly through its transfer-matrix $\mathbf{S}(\omega)$, whereas in the weak-reflector limit its response can be represented by an effective amplitude reflectivity $r_m = |r_m|\, e^{\mathrm{i}\arg r_m}$. The vacuum gaps are of lengths $L_1 = z_0$ and $L_2 = L - z_0 - d$.

2.1. Internal Dielectric Element and Position Conventions

A dielectric slab of thickness d and complex refractive index $n_s(\omega)$ is placed inside the empty cavity at longitudinal position z_c (center of the slab). The front face of the slab is therefore at

$$z_0 \equiv z_c - \frac{d}{2}, \tag{1}$$

so that the vacuum gaps between the mirrors and the slab are

$$L_1 = z_0, \qquad L_2 = L - z_0 - d. \tag{2}$$

In the thin-element limit $d \to 0$, the slab is treated as localized at z_0, so that its geometric thickness is neglected and $L_2 = L - z_0$. Inside the slab, the wavenumber is

$$k_s \equiv n_s(\omega)\,\frac{\omega}{c} = n_s(\omega)\,k, \tag{3}$$

which may be too complex to account for absorption. In the weak-reflector regime, it is also convenient to describe the internal element by an effective complex amplitude reflectivity

$$r_m(\omega) \equiv |r_m(\omega)|\, e^{\mathrm{i}\arg r_m(\omega)}, \qquad 0 < |r_m(\omega)| \ll 1, \tag{4}$$

where $|r_m(\omega)|$ is the reflection amplitude and $\arg r_m(\omega)$ is its phase. For a finite-thickness slab, this phase generally contains both interface-reflection and propagation contributions, i.e., it represents the net phase of the slab's effective reflection response.

2.2. Field Convention and Elementary Matrices

In each uniform region (vacuum or slab), the scalar field is written as a superposition of forward-propagating (+) and backward-propagating (−) waves,

$$E(z) = E^{+}(z)\, e^{+ikz} + E^{-}(z)\, e^{-ikz} \qquad \text{(vacuum)}, \tag{5}$$

$$E_s(z) = E_s^{+}(z)\, e^{+ik_s z} + E_s^{-}(z)\, e^{-ik_s z} \qquad \text{(slab)}. \tag{6}$$

We collect the local amplitudes into state vectors, $(E^{-}(z), E^{+}(z))^{\mathsf{T}}$ for the vacuum and $(E_s^{-}(z), E_s^{+}(z))^{\mathsf{T}}$ for the slab. Transfer matrices relate these vectors between reference planes. Throughout, we use the convention that if two reference planes are ordered from left to right, then the field-amplitude vector at the left plane is obtained from that at the right plane by multiplication with the appropriate transfer-matrix.

Propagation through a homogeneous region of length L with wavenumber k is described by the diagonal matrix

$$\mathbf{P}(k, L) \equiv \begin{pmatrix} e^{ikL} & 0 \\ 0 & e^{-ikL} \end{pmatrix}. \tag{7}$$

At a planar interface between two media with refractive indices n_a (left) and n_b (right), the forward/backward amplitudes are related by an interface matrix

$$\mathbf{I}_{a\to b} \equiv \frac{1}{t_{a\to b}} \begin{pmatrix} 1 & r_{a\to b} \\ r_{a\to b} & 1 \end{pmatrix}, \tag{8}$$

with Fresnel coefficients

$$r_{a\to b} = \frac{n_a - n_b}{n_a + n_b}, \qquad t_{a\to b} = \frac{2n_a}{n_a + n_b}. \tag{9}$$

The slab block $\mathbf{S}(\omega)$ relates the field amplitudes on the two sides of the slab within the same right-to-left transfer-matrix convention used throughout this work:

$$\mathbf{S}(\omega) \equiv \mathbf{I}_{v\to s}\, \mathbf{P}(k_s, d)\, \mathbf{I}_{s\to v}, \tag{10}$$

where v denotes vacuum and s denotes the slab medium.

Each end mirror M_j ($j = 1, 3$) is modeled as a two-port optical element in the standard forward/backward wave transfer-matrix formalism,

$$\mathbf{M}_j \equiv \frac{1}{t_j} \begin{pmatrix} 1 & r_j \\ r_j & 1 \end{pmatrix}, \tag{11}$$

which has the same form as the transfer-matrix of a symmetric interface in layered-media optics [27]. This form is appropriate for standard dielectric mirrors at normal incidence and allows coating phases to be absorbed into the complex coefficients r_j and t_j.

2.3. Total Transfer-Matrix

The total transfer-matrix from the plane just outside M_1 on the input side to the plane just outside M_3 on the output side is

$$\mathbf{M}_{\text{tot}}(\omega) = \mathbf{M}_1(\omega)\, \mathbf{P}(k, L_1)\, \mathbf{S}(\omega)\, \mathbf{P}(k, L_2)\, \mathbf{M}_3(\omega) \equiv \begin{pmatrix} A(\omega) & B(\omega) \\ C(\omega) & D(\omega) \end{pmatrix}. \tag{12}$$

With our transfer-matrix convention, the field amplitudes just outside the cavity satisfy

$$\begin{pmatrix} E_L^- \\ E_L^+ \end{pmatrix} = \mathbf{M}_{\mathrm{tot}}(\omega) \begin{pmatrix} E_R^- \\ E_R^+ \end{pmatrix} \tag{13}$$

where the subscripts L and R indicate fields just to the left of M_1 and just to the right of M_3, respectively. Assuming incidence from the left, one has $E_L^+ = E_{\mathrm{in}}$, $E_L^- = E_{\mathrm{ref}}$, $E_R^+ = E_{\mathrm{out}}$ and $E_R^- = 0$. Equation (13) then gives

$$E_{\mathrm{ref}} = B(\omega)\, E_{\mathrm{out}}, \qquad E_{\mathrm{in}} = D(\omega)\, E_{\mathrm{out}}, \tag{14}$$

so that the complex transmission and reflection coefficients are

$$t(\omega) \equiv \frac{E_{\mathrm{out}}}{E_{\mathrm{in}}} = \frac{1}{D(\omega)}, \qquad r(\omega) \equiv \frac{E_{\mathrm{ref}}}{E_{\mathrm{in}}} = \frac{B(\omega)}{D(\omega)}. \tag{15}$$

The resonances of the composite cavity correspond to complex frequencies $\tilde{\omega}$, at which $t(\omega)$ has poles, i.e.,

$$D(\tilde{\omega}) = 0, \qquad \mathfrak{Im}\, \tilde{\omega} < 0. \tag{16}$$

This pole condition forms the basis for the exact single-slab analysis in Section 3 and for the asymptotic, mode-resolved pole-shift expressions developed in Section 4.

3. Single Internal Slab: Exact Transfer Function and Pole Equation

This section derives the exact transfer function and the corresponding pole equation for a two-mirror cavity containing a single internal dielectric slab of arbitrary thickness and complex refractive index. The derivation proceeds directly from the transfer-matrix framework introduced in Section 2. The resulting expressions form the basis for the weak-reflector asymptotics developed in Section 4.

3.1. Slab Transfer-Matrix in Vacuum

Using the interface convention of Equation (8), the slab block defined in Equation (10) can be written explicitly as

$$\mathbf{S}(\omega) \equiv \begin{pmatrix} A_s(\omega) & B_s(\omega) \\ C_s(\omega) & D_s(\omega) \end{pmatrix}, \tag{17}$$

where the matrix elements take the standard closed form

$$A_s(\omega) = \cos\phi + \mathrm{i}\, \frac{n_s^2 + 1}{2n_s} \sin\phi, \tag{18}$$

$$B_s(\omega) = +\mathrm{i}\, \frac{n_s^2 - 1}{2n_s} \sin\phi, \tag{19}$$

$$C_s(\omega) = -\mathrm{i}\, \frac{n_s^2 - 1}{2n_s} \sin\phi, \tag{20}$$

$$D_s(\omega) = \cos\phi - \mathrm{i}\, \frac{n_s^2 + 1}{2n_s} \sin\phi, \tag{21}$$

with $\phi(\omega) \equiv k_s d = n_s(\omega)\, \omega\, d/c$. These expressions remain valid for complex $n_s(\omega)$ and therefore include slab absorption via $\mathfrak{Im}\, n_s(\omega) > 0$.

3.2. Exact Transmission Amplitude

Using the total transfer-matrix given in Equation (12), the transmission amplitude for left incidence is given by Equation (15). Carrying out the matrix multiplication yields a compact expression for $D(\omega)$

$$D(\omega) = \frac{e^{-ik(L_1+L_2)}}{t_1(\omega)\, t_3(\omega)}\, \mathcal{D}(\omega), \tag{22}$$

where the reduced denominator $\mathcal{D}$ is

$$\mathcal{D}(\omega) = D_s(\omega) + B_s(\omega)\, r_1(\omega)\, e^{i2kL_1} + C_s(\omega)\, r_3(\omega)\, e^{i2kL_2} + A_s(\omega)\, r_1(\omega) r_3(\omega)\, e^{i2k(L_1+L_2)}. \tag{23}$$

An equivalent scattering/boundary-condition derivation of the same reduced denominator is given in Appendix A. Since the prefactor in Equation (22) is nonzero, the transmission amplitude can be written as

$$t(\omega) = \frac{t_1(\omega)\, t_3(\omega)\, e^{ik(L_1+L_2)}}{\mathcal{D}(\omega)}, \tag{24}$$

so the cavity poles are determined entirely by the zeros of the reduced denominator:

$$\mathcal{D}(\tilde{\omega}_\mu) = 0, \qquad \mathfrak{Im}\, \tilde{\omega}_\mu < 0. \tag{25}$$

The full cavity response is thus encoded in the single scalar function $\mathcal{D}(\omega)$. This pole condition determines the complex resonance frequencies $\tilde{\omega}_\mu$ and is the starting point for both the exact analysis of single-slab cavities and the weak-reflector asymptotics of Section 4. As a consistency check, consider the no-slab limit $\mathbf{S} \to \mathbb{I}$, corresponding to setting $A_s = D_s = 1$ and $B_s = C_s = 0$ in Equation (23). Equation (25) then reduces to

$$\mathcal{D}(\tilde{\omega}_\mu) = 1 + r_1(\tilde{\omega}_\mu)\, r_3(\tilde{\omega}_\mu)\, e^{i2\tilde{k}_\mu L} = 0, \qquad \tilde{k}_\mu \equiv \tilde{\omega}_\mu / c. \tag{26}$$

With the present transfer-matrix convention, this is the bare-cavity pole condition. In alternative conventions, where one mirror reflection is assigned an additional π phase, the same condition is equivalently written as

$$1 - r_1(\tilde{\omega}_\mu) r_3(\tilde{\omega}_\mu) e^{i2\tilde{k}_\mu L} = 0. \tag{27}$$

In the opposite limit of a strongly reflecting internal slab, the pole equation (25) describes the emergence of coupled-cavity spectra. The present work focuses on the experimentally common weak-reflector regime, where the empty-cavity longitudinal modes remain well resolved and the slab induces controlled perturbations.

4. Weak-Reflector Asymptotics: First-Order Pole Shift as an Optical Self-Energy

We now extract mode-resolved first-order expressions for the complex pole shift induced by a weak internal reflector. For a high-finesse bare cavity and an internal element whose net amplitude reflectivity is small, the spectrum remains well described by isolated poles in the complex-frequency plane. In this regime, each bare-cavity pole acquires a small complex correction $\delta\tilde{\omega}_\mu$, whose real part gives the resonance frequency shift, while -2 times its imaginary part gives the linewidth change. This correction can be written as an optical self-energy in a one-pole Green-function representation [28], consistent with the standard

view that open-cavity resonances are quasinormal modes with complex eigenfrequencies that coincide with poles of the Green function (and of the scattering response) [29].

4.1. One-Pole Reduction and Self-Energy

Let $\tilde{\omega}_\mu^{(0)}$ denote an isolated pole of the empty two-mirror cavity, with linewidth $\kappa_\mu^{(0)} \equiv -2\,\mathfrak{Im}\,\tilde{\omega}_\mu^{(0)}$ and free spectral range (FSR) $\omega_{\mathrm{FSR}} = \pi c/L$. In the presence of a weak internal reflector, the pole shifts to

$$\tilde{\omega}_\mu = \tilde{\omega}_\mu^{(0)} + \delta\tilde{\omega}_\mu, \qquad \delta\tilde{\omega}_\mu \in \mathbb{C}. \tag{28}$$

Near $\tilde{\omega}_\mu^{(0)}$, the transmission amplitude admits a one-pole approximation of the form

$$t(\omega) \;\propto\; \frac{1}{\omega - \tilde{\omega}_\mu^{(0)} - \Sigma_\mu(\omega)}, \tag{29}$$

where $\Sigma_\mu(\omega)$ is the optical self-energy, i.e., the complex, frequency-dependent correction induced by the internal element to the bare-cavity pole. In the weak-reflector regime, $\Sigma_\mu(\omega)$ varies weakly across a single resonance, so to leading order

$$\delta\tilde{\omega}_\mu \simeq \Sigma_\mu\Big(\tilde{\omega}_\mu^{(0)}\Big). \tag{30}$$

Writing

$$\delta\omega_\mu \equiv \mathfrak{Re}\;\delta\tilde{\omega}_\mu, \qquad \delta\kappa_\mu \equiv -2\;\mathfrak{Im}\;\delta\tilde{\omega}_\mu, \tag{31}$$

defines the mode pulling $\delta\omega_\mu$ and the linewidth change $\delta\kappa_\mu$.

4.2. Weak-Reflector Limit: First-Order Complex Shift for a Single Internal Element

To study the weak-reflector asymptotics, we start by parameterizing the net internal reflection via the effective amplitude $r_m(\omega) = B_s(\omega)/D_s(\omega)$, analogously to Equation (15), with B_s and D_s the transfer-matrix elements defined by Equation (17). This complex quantity can be decomposed according to Equation (4), with the magnitude fulfilling $|r_m| \ll 1$ in the pertinent weak-reflector regime. Expanding the exact reduced denominator of Equation (23) to first order in $|r_m|$ gives

$$\mathcal{D}(\omega, z_0) = \mathcal{D}_0(\omega) + \mathcal{D}_1(\omega, z_0) + \mathcal{O}(r_m^2)\,, \tag{32}$$

where

$$\mathcal{D}_0(\omega) = 1 + r_1(\omega)\, r_3(\omega)\, e^{i2kL} \tag{33}$$

is the empty-cavity denominator and

$$\mathcal{D}_1(\omega, z_0) = r_m(\omega)\, r_1(\omega)\, e^{i2kz_0} - r_m(\omega)\, r_3(\omega)\, e^{i2k(L-z_0)} \tag{34}$$

is the first-order correction, written as the coherent sum of the two mirror-side scattering paths. Note that the small parameter in the expansion is the reflection amplitude $|r_m|$, whereas the reflection phase $\arg r_m$ is retained and may include finite-thickness phase accumulation. Appendix B contains a short derivation of this first-order form. Apart from $|r_m|$ being considerably smaller than unity (cf. Figure A2), the validity of the first-order approximation is further contingent on the induced pole correction to remaining small compared to the separation from neighboring poles, so that the selected mode remains isolated.

Linearizing the pole condition around $\tilde{\omega}_\mu^{(0)}$ gives

$$\delta\tilde{\omega}_\mu(z_0) \simeq -\,\mathrm{i}\,\frac{c}{2L}\,r_m(\tilde{\omega}_\mu^{(0)})\left[r_1(\tilde{\omega}_\mu^{(0)})\,e^{i2\tilde{k}_\mu^{(0)}z_0} - r_3(\tilde{\omega}_\mu^{(0)})\,e^{i2\tilde{k}_\mu^{(0)}(L-z_0)}\right], \tag{35}$$

where $\tilde{k}_\mu^{(0)} \equiv \tilde{\omega}_\mu^{(0)}/c$. Using the empty-cavity pole condition

$$r_1(\tilde{\omega}_\mu^{(0)})\,r_3(\tilde{\omega}_\mu^{(0)})\,e^{i2\tilde{k}_\mu^{(0)}L} = -1, \tag{36}$$

one may eliminate r_1 in favour of r_3, which yields

$$\delta\tilde{\omega}_\mu(z_0) \simeq \mathrm{i}\,\frac{c}{2L}\,r_m(\tilde{\omega}_\mu^{(0)})\left[\frac{e^{-i2\tilde{k}_\mu^{(0)}(L-z_0)}}{r_3(\tilde{\omega}_\mu^{(0)})} + r_3(\tilde{\omega}_\mu^{(0)})\,e^{i2\tilde{k}_\mu^{(0)}(L-z_0)}\right]. \tag{37}$$

It is convenient to define

$$\zeta_\mu(z_0) \equiv r_m(\tilde{\omega}_\mu^{(0)})\left[\frac{e^{-i2\tilde{k}_\mu^{(0)}(L-z_0)}}{r_3(\tilde{\omega}_\mu^{(0)})} + r_3(\tilde{\omega}_\mu^{(0)})\,e^{i2\tilde{k}_\mu^{(0)}(L-z_0)}\right], \tag{38}$$

so that the pole shift takes the compact form

$$\delta\tilde{\omega}_\mu(z_0) = \mathrm{i}\,\frac{c}{2L}\,\zeta_\mu(z_0). \tag{39}$$

Combining Equations (31) and (39) gives

$$\delta\omega_\mu(z_0) = -\frac{c}{2L}\,\mathfrak{Im}\;\zeta_\mu(z_0), \tag{40}$$

$$\delta\kappa_\mu(z_0) = -\frac{c}{L}\,\mathfrak{Re}\;\zeta_\mu(z_0). \tag{41}$$

Equations (40) and (41) are the generic first-order weak-reflector relations consistent with the exact transfer-matrix denominator. For a two-sided high-finesse cavity, the first-order pole shift is therefore governed by the coherent sum of two mirror-side scattering contributions encoded in $\zeta_\mu(z_0)$. For a finite-thickness weak slab, the same first-order strategy applies, but the relevant linear term in the expansion of the exact reduced denominator from Equation (23) must be obtained directly rather than by identifying the slab with a thin effective reflector a priori. Equations (40) and (41) also give direct placement criteria in terms of the complex quantity $\zeta_\mu(z_0)$. Purely dispersive first-order operation requires $\mathfrak{Re}\;\zeta_\mu(z_0) = 0$, whereas purely dissipative first-order operation requires $\mathfrak{Im}\;\zeta_\mu(z_0) = 0$. These conditions identify the slab positions at which the first-order linewidth change or the first-order frequency shift vanishes, respectively. Positions where both quantities are small correspond to a weak net perturbation of the cavity resonance.

4.3. Parameter Extraction from Measured Resonance Traces

Here we assume that the internal element is present inside the cavity and show how the effective first-order weak-reflector response can be inferred from measured resonance traces. This provides a model-light way to extract the dominant complex scattering response without first specifying a full microscopic slab model. Equations (40) and (41) imply that scanning the element position maps each empty-cavity mode μ onto a trajectory in the plane $(\delta\omega_\mu, \delta\kappa_\mu)$ determined by the two-path interference encoded in $\zeta_\mu(z_0)$. The following details the steps towards parameter extraction from such a trajectory.

Step 1: Measure resonance shifts and linewidth changes.

For a fixed longitudinal mode μ, record the fitted resonance frequency and linewidth $(\omega_\mu(z_i), \kappa_\mu(z_i))$ at a set of positions $\{z_i\}$. Define shifts relative to a reference position:

$$\delta\omega_\mu(z_i) = \omega_\mu(z_i) - \bar{\omega}_\mu, \qquad \delta\kappa_\mu(z_i) = \kappa_\mu(z_i) - \bar{\kappa}_\mu. \tag{42}$$

If the reference values are not the empty-cavity values, the reconstructed ζ_μ is determined up to an additive constant, which can be included as a fit offset.

Step 2: Reconstruct the effective first-order correction.

Using Equations (40) and (41), combine the measured data into the complex quantity

$$\zeta_\mu(z_i) = -\frac{L}{c}\,\delta\kappa_\mu(z_i) - \mathrm{i}\,\frac{2L}{c}\,\delta\omega_\mu(z_i). \tag{43}$$

This reconstructs the first-order pole correction pointwise, up to the chosen reference offset, and separates the measured response into its dispersive and linewidth-changing components.

Step 3: Fit the first-order two-path form.

Fit the reconstructed $\zeta_\mu(z_i)$ to the position dependence implied by Equation (38), which has the explicit two-path form $\zeta_\mu(z_0) = A_\mu e^{2i\tilde{k}_\mu^{(0)} z_0} + B_\mu e^{-2i\tilde{k}_\mu^{(0)} z_0} + C_\mu$. The complex coefficients (A_μ, B_μ, C_μ) absorb the combined effects of the internal element and the cavity response. If independent empty-cavity calibration data (L, $\tilde{\omega}_\mu^{(0)}$ or equivalently $\tilde{k}_\mu^{(0)}$, and mirror coefficients) are additionally available, the fitted coefficients may be related to an effective internal reflectivity referenced to the calibrated empty-cavity response. Without such a calibration, the fit still determines the composite coefficients entering the first-order two-path model, but not necessarily a unique physical decomposition.

Significant deviations from the fitted two-path model indicate breakdown of the isolated-pole first-order approximation, for example because $|r_m|$ is no longer small, because higher-order multiple scattering becomes important, or because additional nearby resonances must be retained. In such cases, the exact pole condition expressed by Equation (25) should be used directly.

4.4. Cavity Calibration from an Empty-Cavity Scan and Prediction with an Inserted Slab

Unlike the "inverse" workflow of Section 4.3, which reconstructs the effective first-order correction directly from perturbed resonance traces, the alternative workflow begins by calibrating the empty cavity itself. The obtained cavity parameters are then inserted into a forward model to predict the resonance shifts and linewidth changes produced by an inserted slab. The weak-reflector prediction exposes the two-path interference mechanism underlying the slab-induced ridge motion, while the exact transfer-matrix calculation retains finite-thickness phase accumulation and higher-order internal scattering. Below we elaborate on these two steps of the prediction procedure.

Step 1: Empty-cavity calibration.

From a scan of the transmitted intensity over several resonances, one extracts the FSR ω_{FSR} and the linewidths $\kappa_\mu^{(0)}$, typically via Lorentzian fits [30]. This fixes the cavity length $L = \pi c/\omega_{\mathrm{FSR}}$ and, over a sufficiently narrow spectral range, the corresponding finesse $\mathcal{F} = \omega_{\mathrm{FSR}}/\kappa^{(0)}$. The peak heights (and, when available, simultaneous reflection data) constrain the coupling asymmetry and the effective round-trip loss, yielding a consistent set of mirror parameters (r_1, t_1, r_3, t_3) for forward modeling.

Step 2: Forward prediction with an inserted slab.

Given (L, r_1, t_1, r_3, t_3), inserting a slab with parameters $(n_s(\omega), d)$ at position z_0 yields the exact transmission $t(\omega)$ via Equation (24). Repeating this calculation for a set of positions z_0 produces a reconstructed transmission map $T(\omega, z_0) = |t(\omega; z_0)|^2$, from which the predicted shifts $\delta\omega_\mu(z_0)$ and linewidth changes $\delta\kappa_\mu(z_0)$ can be extracted by the same fitting procedure used in the experiment. Experimentally, the slab may be translated with a calibrated positioning stage while corresponding cavity transmission spectra are recorded. Resonance fits yield the position-dependent shifts $\delta\omega_\mu(z_0)$ and linewidth changes $\delta\kappa_\mu(z_0)$. Their modulation amplitudes and sensitivity to displacement provide directly measurable performance metrics, while deviations between the measured and predicted $(\delta\omega, \delta\kappa)$ reveal higher-order multiple scattering, neighboring-pole effects, or additional loss mechanisms beyond the one-dimensional model.

Figure 2 summarizes the comparison between the weak-reflector approximation and the exact transfer-matrix prediction for an internal dielectric slab whose position relative to the cavity center, Δz_c, is scanned over one optical wavelength, here taken to be λ = 532 nm. The cavity parameters used for this prediction are L = 42 mm, corresponding to $\nu_{\mathrm{FSR}} = \omega_{\mathrm{FSR}}/2\pi \approx 3.569$ GHz, and the empty cavity linewidth of $\kappa^{(0)}/2\pi = 305$ kHz. Assuming a symmetric cavity and transmission through the mirrors to be the only loss channel, $\kappa_j = \nu_{\mathrm{FSR}}(1 - |r_j|^2)$ $(j = 1, 3)$ yields $|r_1| = |r_3| \approx 0.999865$. The reflection phases are fixed by the chosen transfer-matrix convention or equivalently absorbed into the calibrated empty-cavity phase reference. The slab thickness and refractive index are d = 200 µm and $n_s = 1.45 + 0.0\mathrm{i}$, respectively. This yields an optical phase of 0.7086 rad (mod 2π) accumulated across the slab. The corresponding effective amplitude reflectivity is $|r_m| = |B_s/D_s| \approx 0.24$, placing the example in the regime of moderately weak reflectors, rather than deeply in the limit $|r_m| \ll 1$.

Panels (a) and (b) compare the corresponding transmission maps in the normalized coordinates $\Delta\nu/\nu_{\mathrm{FSR}}$ and $\Delta z_c/\lambda$. Panel (a) is constructed from the first-order mode-resolved pole shift and linewidth correction, whereas panel (b) is evaluated directly from the exact transfer function in Equation (24). The resonance brightness in (a) depends on the corresponding linewidth, normalization and rendering, which leads to ranges of Δz_c for which the transmission is not prominent. Panel (c) removes this finite linewidth and compares only the extracted resonance-center trajectories, or ridges, for the four visible cavity modes. Both models predict periodic position-dependent mode pulling as the slab is translated, with the weak-reflector model reproducing well the overall periodicity and scale of the ridge motion. In particular, the ridge trajectories are generally not in phase from one visible cavity mode to the next. All such trajectories share the same displacement period of $\lambda/2$, but each carries its own mode-dependent phase through the complex coefficient $\zeta_\mu(z_0)$ evaluated at the corresponding bare-cavity pole. As a result, neighboring modes are phase-shifted relative to one another and, for the symmetric cavity considered here, can appear approximately in antiphase near the cavity center, so that a crest of one trajectory aligns with a trough of the next. This phase relation is contained in the weak-model formula. Still, the deviations from the exact transfer-matrix result are small but systematic: the exact ridges exhibit a modest phase offset and slight shape deformation, most visible near the turning points and in the enlarged segment of panel (b). These differences arise from finite-thickness phase accumulation and higher-order multiple scattering. In particular, the weak-reflector model breaks down as the slab thickness approaches the condition $n_s d = (2q + 1)\lambda/4$, $q \in \mathbb{Z}$. See Appendix C for an extensive discussion on the model limitations.

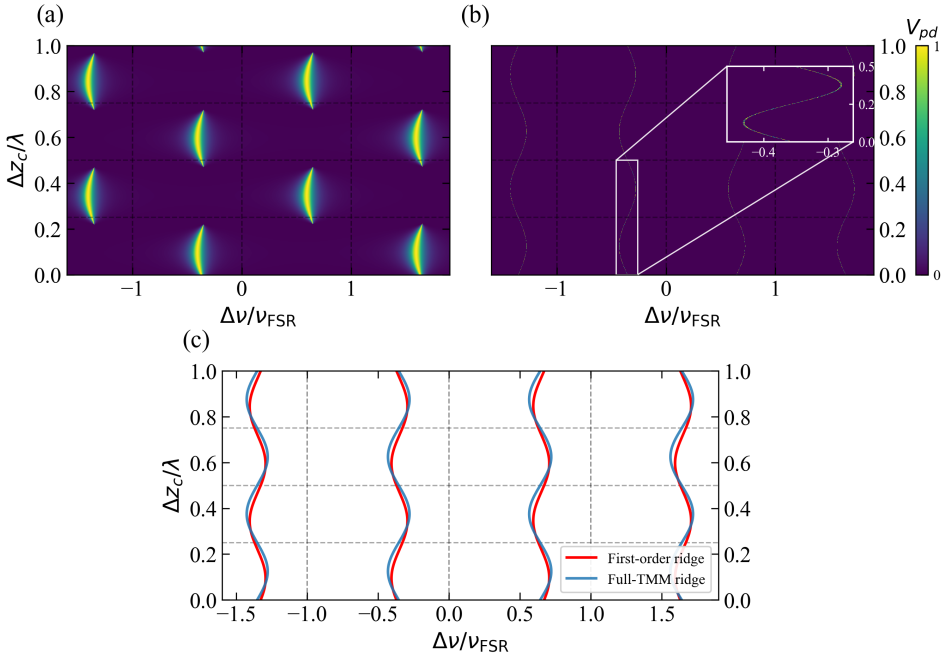


Figure 2. Comparison of weak-reflector and exact transfer-matrix predictions for a 200 µm thick intracavity slab, the position of which Δz_c is scanned relative to the cavity center. The slab has a refractive index of $1.45 + 0.0\mathrm{i}$ at 532 nm and is a moderately weak reflector with $|r_m| \approx 0.24$. (**a**) First-order weak-reflector transmission map constructed from the mode-resolved pole shift and linewidth correction. (**b**) Exact transfer-matrix transmission map evaluated from Equation (24). Inset: Enlarged view of one oscillation segment of the exact resonance pattern. (**c**) Weak-model (red) and full-TMM (blue) ridge trajectories for the visible cavity modes, with the finite linewidth removed.

4.5. An Example: A Dual-Wavelength Scheme for Absorption-Free Detection

As a practical application of the first-order framework, consider the following setup used to infer the presence of a semitransparent slab inside the cavity in a way that minimizes the probability of absorption by said object. The scheme includes two fields of potentially significantly different wavelengths. The "locking" field (at ω_L) is locked to one cavity resonance, thus providing a frequency reference, whereas a weak "interrogation" field (at ω_I) is locked to the locking field with a frequency offset ω_{off} and tuned near a different cavity resonance. The exact detuning Δ_I of the interrogation field is contingent on the object's presence, owing to the object-induced pulling of the respective cavity mode frequency (cf. Figure 3a). The larger $|\Delta_I|$, the larger the cavity reflectivity $\mathcal{R}_I = 1 - b \cdot (\kappa_\mu^{(I)})^2/[(\kappa_\mu^{(I)})^2 + 4\,\Delta_I^2]$ for this field, with $0 \leq b \leq 1$ a scaling factor dependent on the cavity coupling efficiency and achieved mode-matching [31]. In particular, as $|\Delta_I| \to \infty$, $\mathcal{R}_I \to 1$. In that case, the intracavity amplitude of the interrogation field, and thus also the probability of its absorption, tend to zero. Of course, $|\Delta_I|$ is experimentally bound from above by $\omega_{\mathrm{FSR}}/2$, but for a high-finesse cavity $\mathcal{R}_I$ can still be made extremely small.

To identify suitable working points of a doubly resonant cavity for the outlined purpose, we start by noting the slab can be characterized by a frequency-dependent complex refractive index

$$n_s(\omega) = n'(\omega) + \mathrm{i}\, n''(\omega). \tag{44}$$

For both ω_L and ω_I, the first-order weak-reflector correction is obtained directly from the formulas in Section 4.2, by evaluating $\zeta_\mu(z_0)$, $\delta\omega_\mu(z_0)$, and $\delta\kappa_\mu(z_0)$ at the corresponding bare-cavity pole $\tilde{\omega}_\mu^{(0,\alpha)}$, $\alpha \in \{L, I\}$. Discriminating the object's presence or absence while simultaneously minimizing absorption of the field at ω_I requires $|\Delta_I| \gg \kappa_\mu^{(I)}$ upon the inclusion of the object inside the cavity. Assuming the locks are maintained, and both

fields are resonant with their respective modes when the cavity is empty, this will be met if the object-induced frequency shifts of the two modes fulfill $|\delta\omega_\mu^{(I)} - \delta\omega_\mu^{(L)}| \gg \kappa_\mu^{(I)}$. Generally speaking, this criterion takes into account the concomitant change in the linewidth due to object absorption, $\delta\kappa_\mu^{(I)}$, but the effect is mitigated if the slab is placed at the predominantly dispersive operating point, where $\mathfrak{Re}\ \zeta_\mu^{(I)}(z_0) \approx 0$, i.e., $\delta\kappa_\mu^{(I)}(z_0) \approx 0$. In practice, maintaining the locks dictates negligible mode pulling and linewidth change at ω_L, which can be cast as requiring $|\delta\omega_\mu^{(L)}(z_0)| \leq \Delta\omega_L^{\mathrm{tol}}$ and $|\delta\kappa_\mu^{(L)}(z_0)| \leq \Delta\kappa_L^{\mathrm{tol}}$, where the right-hand sides correspond to certain experimental tolerances. This can, in turn, be facilitated by $|r_m(\omega_L)| \ll 1$ and $n''(\omega_L) \approx 0$. Putting everything together, a suitable design strategy is to choose the slab material and coating such that

$$|r_m(\omega_L)| \ll |r_m(\omega_I)|, \qquad n''(\omega_L) \ll n''(\omega_I), \tag{45}$$

and then select z_0 so that the two-path interference encoded in $\zeta_\mu^{(L)}$ keeps the locking field only weakly perturbed, while $\zeta_\mu^{(I)}$ produces the desired interrogation field. One way to achieve this is to have the interrogation wavelength be two times larger than that of the locking field, as indicated in Figure 3b. Finally, the design can be verified simultaneously at both wavelengths using the exact transfer function from Equation (24), with $L_1 = z_0$, $L_2 = L - z_0 - d$, and the wavelength-dependent slab matrix $\mathbf{S}(\omega)$. For coated slabs, $\mathbf{S}(\omega)$ is replaced by the transfer-matrix of the full coating–slab stack.

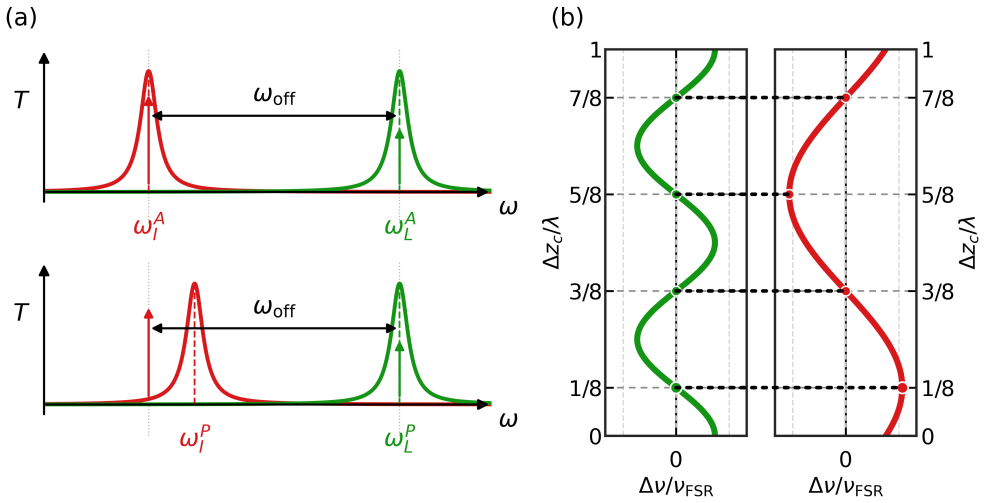


Figure 3. Doubly resonant cavity scheme for absorption-free detection. (**a**) The locking field (green) is locked to one cavity resonance, while the interrogation field (red) is frequency-locked to the locking field with an offset ω_{off} and is tuned near a second cavity resonance. If the cavity is empty (top panel, superscript A for "absent"), the interrogation field is resonant with the second cavity mode, whereas if the object is present inside (bottom panel, superscript P), it induces relative detuning. (**b**) If the interrogation field wavelength is two times that of the locking field, every other object position leading to a zero frequency shift in the locking mode (horizontal dashed lines) corresponds to a maximal shift in the interrogation mode, enabling the scenario in (**a**).

5. Multiple Internal Reflectors: Pole Parametrization and the Three-Mirror Geometry

We now extend the single-slab analysis to cavities containing multiple partially reflecting internal elements. In the transfer-matrix formulation, each new reflector contributes an additional 2×2 block, and the total cavity response is obtained by multiplying the corresponding matrices in the appropriate order. Although the algebra grows in complexity, the resonances are still determined by the zeros of the reduced denominator in

the complex-frequency plane, with the internal reflectors producing multiple coupled poles. This section develops a compact parametrization of these poles and highlights the three-mirror configuration as an important special case.

Consider a cavity containing N internal dielectric elements, each characterized by a slab matrix $\mathbf{S}_j(\omega)$ and separated by vacuum gaps of lengths L_j with propagation matrices $\mathbf{P}(k, L_j)$. The total transfer-matrix takes the form

$$\mathbf{M}_{\mathrm{tot}}(\omega) = \mathbf{M}_1(\omega) \left[\prod_{j=1}^{N} \mathbf{P}(k, L_j)\, \mathbf{S}_j(\omega) \right] \mathbf{P}(k, L_{N+1})\, \mathbf{M}_3(\omega), \tag{46}$$

where the product is ordered from left to right along the optical axis. Writing $\mathbf{M}_{\mathrm{tot}}(\omega)$ in the 2×2 form introduced in Section 2.3, the transmission amplitude retains the same form as in Equation (15). For $N > 1$, the reduced denominator $\mathcal{D}^{(N)}(\omega)$ contains additional interference terms arising from the multiple internal reflection pathways introduced by each element. Physically, each internal reflector creates an additional sub-cavity, the resonances of which hybridize with those of the bare FP cavity. The resulting poles in the complex-frequency plane can therefore be interpreted as the coupled resonances of these interacting sub-cavities. A convenient way to express this structure is to expand the denominator in powers of the effective internal reflectivities $r_{m,j}(\omega)$ of the j-th internal element:

$$\mathcal{D}^{(N)}(\omega) = \mathcal{D}_0(\omega) + \sum_j \mathcal{D}_j(\omega)\, r_{m,j}(\omega) + \sum_{j<k} \mathcal{D}_{jk}(\omega)\, r_{m,j}(\omega)\, r_{m,k}(\omega) + \ldots, \tag{47}$$

where each coefficient $\mathcal{D}_{j_1 \cdots j_p}(\omega)$ is a smooth function determined by the propagation phases and mirror parameters. The linear terms describe single-reflection processes involving one internal element, while higher-order terms encode multiple scattering between different internal reflectors.

In the weak-reflector regime, one may seek each pole in the form given by Equation (28), where $\tilde{\omega}_\mu^{(0)}$ is the corresponding empty-cavity pole and $|\delta\tilde{\omega}_\mu| \ll |\tilde{\omega}_\mu^{(0)}|$. Expanding $\mathcal{D}^{(N)}(\tilde{\omega}_\mu)$ to the first order around $\tilde{\omega}_\mu^{(0)}$ gives a perturbative pole correction that may be written formally as

$$\delta\tilde{\omega}_\mu \simeq \Sigma_\mu^{(N)}\left(\tilde{\omega}_\mu^{(0)}\right), \tag{48}$$

leading to

$$\tilde{\omega}_\mu \simeq \tilde{\omega}_\mu^{(0)} + \Sigma_\mu^{(N)}\left(\tilde{\omega}_\mu^{(0)}\right), \tag{49}$$

where $\Sigma_\mu^{(N)}$ collects the sum of single-reflector contributions together with multiple-scattering corrections among internal elements. For $N = 1$, this formal self-energy reduces to the first-order result of Section 4, i.e., $\Sigma_\mu^{(1)}(\tilde{\omega}_\mu^{(0)}) = \mathrm{i}(c/2L)\, \zeta_\mu(z_0)$.

As the internal reflectivities increase, the higher-order terms become non-negligible, reflecting multiple scattering among the internal elements and giving rise to hybridized poles and avoided crossings characteristic of coupled resonators.

This parametrization provides a unified language for describing composite FP structures: the resonance spectrum can be viewed as a set of hybridized modes, positions and linewidths of which evolve continuously as the reflectivities, positions, or material properties of the internal elements are varied.

5.1. Two Internal Reflectors: Etalon-like Internal Structure

For $N = 2$ internal reflectors (two membranes or slabs), the internal region between them forms an etalon whose phase is controlled by their separation, so the effective internal

response becomes frequency dependent. In the pole-based language introduced above, the reduced denominator may be organized as

$$\mathcal{D}^{(2)}(\omega) = \mathcal{D}_0(\omega) + \mathcal{D}_1(\omega)\, r_{m,1}(\omega) + \mathcal{D}_2(\omega)\, r_{m,2}(\omega) + \mathcal{D}_{12}(\omega)\, r_{m,1}(\omega)\, r_{m,2}(\omega) + \ldots, \tag{50}$$

where the mixed term $\propto r_{m,1} r_{m,2}$ is the lowest-order signature of mutual multiple scattering between the two internal elements. The additional separation-dependent phase gives the effective correction $\Sigma_\mu^{(2)}(\omega)$ a richer frequency dependence than in the one-reflector case. Perturbatively, the corresponding pole frequency may be written as

$$\tilde{\omega}_\mu \simeq \tilde{\omega}_\mu^{(0)} + \Sigma_{\mu,1}\Big(\tilde{\omega}_\mu^{(0)}\Big) + \Sigma_{\mu,2}\Big(\tilde{\omega}_\mu^{(0)}\Big) + \Sigma_{\mu,12}\Big(\tilde{\omega}_\mu^{(0)}\Big), \tag{51}$$

where $\Sigma_{\mu,1}$ and $\Sigma_{\mu,2}$ are the single-reflector contributions and $\Sigma_{\mu,12}$ denotes the mixed correction arising from multiple scattering between the two internal elements.

In this language, the resonance frequency structures studied in two-membrane and related multi-membrane cavity systems [15–18] can be interpreted as the real parts of the complex poles determined by the full pole condition, while the same calculation simultaneously yields the imaginary parts and hence the linewidth changes. Representative examples of this richer pole behaviour are shown later in the pole-tracking results of Figure 4.

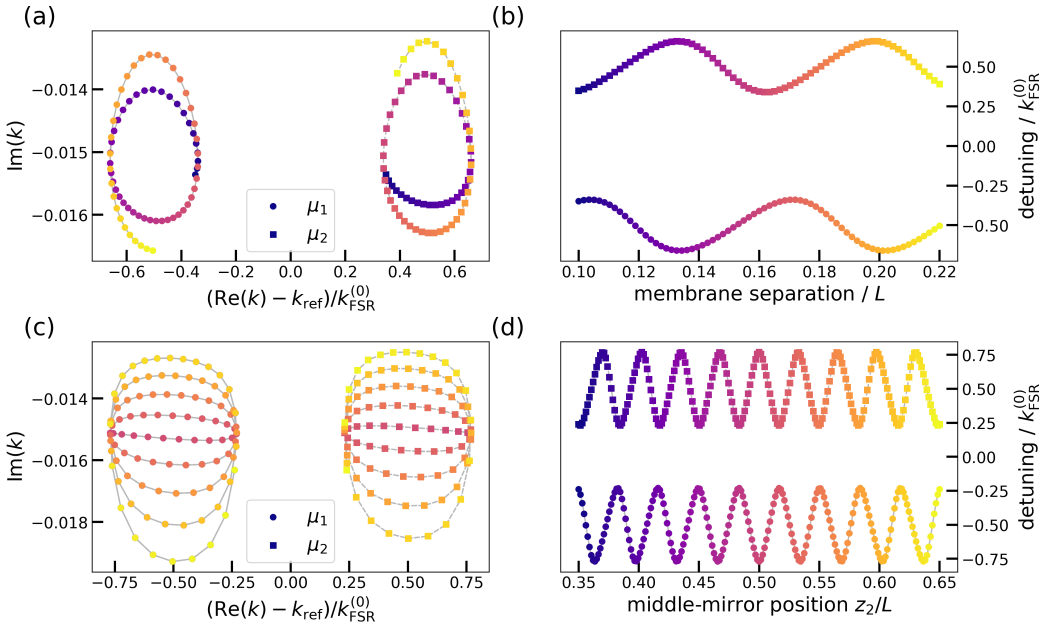


Figure 4. Direct pole tracking under parameter sweeps. (**a**,**b**): two internal membranes, with membrane separation swept; (**c**,**d**) a three-mirror cavity, with the middle-mirror position swept. Two adjacent resonances, μ_1 and μ_2, are tracked in both cases. Left column: trajectories in the complex wavenumber plane k, plotted as $\mathfrak{Im}\, k$ versus the normalized detuning $(\mathfrak{Re}\, k - k_{\mathrm{ref}})/k_{\mathrm{FSR}}^{(0)}$, where $k_{\mathrm{FSR}}^{(0)} = \pi/L$ and k_{ref} is a real reference wavenumber. Right column: corresponding normalized detunings versus the swept parameter. As a visual guide, the traces are color-coded according to the parameter value, indicated on the abscissa of panels (**b**,**d**).

5.2. Three-Mirror Geometry

An important special case of the general internal-element formalism is the linear three-mirror cavity, obtained when the internal slab is replaced by a lumped middle mirror with amplitude coefficients (r_2, t_2). In that limit, the internal-element transfer-matrix is

$$\mathbf{M}_2(\omega) \equiv \frac{1}{t_2(\omega)} \begin{pmatrix} 1 & r_2(\omega) \\ r_2(\omega) & 1 \end{pmatrix}, \tag{52}$$

and the total cavity transfer-matrix becomes

$$\mathbf{M}_{3\mathrm{m}}(\omega) = \mathbf{M}_1(\omega)\,\mathbf{P}(k, L_1)\,\mathbf{M}_2(\omega)\,\mathbf{P}(k, L_2)\,\mathbf{M}_3(\omega). \tag{53}$$

Carrying out the matrix multiplication gives the three-mirror reduced denominator

$$\mathcal{D}_{3\mathrm{m}}(\omega) = 1 + r_1(\omega)r_2(\omega)e^{i2kL_1} + r_2(\omega)r_3(\omega)e^{i2kL_2} + r_1(\omega)r_3(\omega)e^{i2k(L_1+L_2)}. \tag{54}$$

The pole frequencies $\tilde{\omega}_\mu$ are therefore determined by $\mathcal{D}_{3\mathrm{m}}(\tilde{\omega}_\mu) = 0$, or explicitly,

$$1 + r_1(\tilde{\omega}_\mu)r_2(\tilde{\omega}_\mu)e^{i2\tilde{k}_\mu L_1} + r_2(\tilde{\omega}_\mu)r_3(\tilde{\omega}_\mu)e^{i2\tilde{k}_\mu L_2} + r_1(\tilde{\omega}_\mu)r_3(\tilde{\omega}_\mu)e^{i2\tilde{k}_\mu(L_1+L_2)} = 0. \tag{55}$$

This form makes clear which parameters control the hybridized spectrum: the two sub-cavity lengths L_1 and L_2 set the uncoupled resonance phases, while the middle-mirror reflectivity r_2 controls their coupling. When the two sub-cavity resonances are far apart, the poles remain close to those of the uncoupled sections. When they are brought close to one another, Equation (55) yields a pair of nearby hybridized poles, i.e., a resonance doublet, the splitting and linewidth asymmetry of which are governed by the middle mirror. Thus, the familiar normal-mode splitting of a three-mirror cavity appears here as the pole-level manifestation of coupled-resonator hybridization. Equation (55) connects directly to coupled-cavity and three-mirror analyses in the literature [7,8,14,32], while embedding them in the broader pole-based framework developed here. Representative pole trajectories for this regime are shown in Figure 4.

5.3. Pole Tracking Under Parameter Sweeps

Pole trajectories follow directly from the condition $\mathcal{D}(\tilde{\omega}; s) = 0$, where s denotes a swept parameter such as an internal position, reflectivity, thickness, or loss. In practice, one computes $\tilde{\omega}_\mu$ at a reference value s_0 by solving the coupled real equations $\mathfrak{Re}\,\mathcal{D}(\tilde{\omega}; s_0) = 0$, and $\mathfrak{Im}\,\mathcal{D}(\tilde{\omega}; s_0) = 0$, for the complex frequency $\tilde{\omega}$ and retaining the pole in the lower half-plane, $\mathfrak{Im}\,\tilde{\omega}_\mu < 0$. Since the transfer-matrix element $D(\omega)$ differs from the reduced denominator $\mathcal{D}(\omega)$ only by a nonzero analytic prefactor, either form may be used to determine the pole set. The selected swept parameter is then varied step by step, $s_0 \to s_1 \to \ldots$, and each pole found at s_i is used as the initial guess for the solver at s_{i+1}. For a position sweep, one may take $s = \Delta z$, so that translating an internal reflector changes adjacent gaps according to $L_j \mapsto L_j + \Delta z$ and $L_{j+1} \mapsto L_{j+1} - \Delta z$. This continuation procedure yields trajectories $\tilde{\omega}_\mu(s) = \omega_\mu(s) - \mathrm{i}\,\kappa_\mu(s)/2$, which exhibit hybridization and avoided crossings.

Representative numerical pole trajectories obtained by continuation are shown in Figure 4 for two internal membranes with the membrane separation varied [panels (a) and (b)], and a three-mirror cavity with the middle-mirror position varied [panels (c) and (d)]. For each sweep, the continuation algorithm is initialized at two neighbouring resonant poles, μ_1 and μ_2, and then follows their motion as the pertinent parameter is varied. Panels (a) and (c) show the pole trajectories in the complex wavenumber plane, while (b) and

(d) show the corresponding normalized detunings as functions of the swept parameter. Poles are obtained from $\mathcal{D}(k) = 0$ and direct numerical pole tracking is performed in a dimensionless 1D model: $c = L = 1$. The detunings are plotted relative to a real reference wavenumber $k_{\mathrm{ref}} = 30\pi/L$, and normalized to the empty-cavity FSR in wavenumber, $k_{\mathrm{FSR}}^{(0)} = \pi/L$. These normalized wavenumber detunings are directly related to the linear-frequency detunings $\Delta\nu/\nu_{\mathrm{FSR}}^{(0)}$ via $\nu = ck/(2\pi)$. Both end mirrors are taken identical and lossless with amplitude reflectivity $r_{\mathrm{end}} = 0.985$. The pole condition then becomes $1 + r_{\mathrm{end}}^2 e^{i2kL} = 0$, implying in turn that $\Im\mathrm{m}\, k = \ln(r_{\mathrm{end}})/L < 0$. Internal elements are represented by symmetric lumped reflectors with amplitude reflectivities $r_{\mathrm{mem}} = 0.25$ for the two-membrane system and $r_{\mathrm{mid}} = 0.75$ for the three-mirror system, respectively.

The pole trajectories shown in Figure 4 indicate how strongly a resonance frequency or linewidth responds to a controlled change of an internal-cavity parameter and can be used in practice to follow avoided crossings or mode hybridization as the internal reflector parameters are varied. The continuation procedure can be interpreted locally by differentiating the pole condition with respect to the swept parameter. For a pole satisfying $\mathcal{D}(\tilde{\omega}_\mu(s); s) = 0$, implicit differentiation gives

$$\frac{d\tilde{\omega}_\mu}{ds} = -\left.\frac{\partial_s \mathcal{D}(\omega; s)}{\partial_\omega \mathcal{D}(\omega; s)}\right|_{\omega=\tilde{\omega}_\mu(s)}. \tag{56}$$

Here, $\partial_\omega \mathcal{D}$ is the local slope of the pole equation, while $\partial_s \mathcal{D}$ identifies the part of the optical response that is changed by the sweep. For a translation of an internal slab, the adjacent propagation lengths change with opposite signs, so the sensitivity is controlled by the relative phase of the two mirror-side contributions. By contrast, a reflectivity sweep differentiates the scattering amplitudes themselves, whereas thickness, refractive index, and absorption sweeps enter through the slab matrix elements. Equation (56) applies to a simple pole, for which $\partial_\omega \mathcal{D}(\tilde{\omega}_\mu(s); s) \neq 0$. The corresponding explicit forms of $\partial_s \mathcal{D}$, and the modification required when this simple-pole condition fails, are given in Appendix D.

6. Conclusions

We have developed a pole-based framework for analyzing Fabry–Pérot cavities containing internal dielectric structures. Starting from the transfer-matrix formulation, we derive closed-form expressions for the complex transmission of a cavity with a single internal slab of arbitrary thickness, complex refractive index, and longitudinal placement. The resulting reduced denominator $\mathcal{D}(\omega)$ provides a compact description of the cavity resonances through its poles $\tilde{\omega}_\mu$ in the complex-frequency plane.

Specifically, we have shown that, in the regime of a weakly reflecting slab, the first-order complex correction to the poles encapsulates and approximates well both the cavity resonance frequency and linewidth modifications. As such, the full cavity dynamics under a change of a given slab parameter can represented by a trajectory in the complex plane. Assuming the empty cavity response is known, the actual cavity parameters can then easily be estimated if the slab parameter is independently measured or controlled, and vice versa. This also facilitates fine-tuning the composite system response, e.g., with regards to the slab position along the cavity axis in doubly resonant cavities.

We have also extended the pole-based description to multiple internal reflectors, in which case each internal element introduces an additional sub-cavity whose resonances hybridize with those of the bare FP cavity. The resulting coupled-pole structure provides a description of composite FP elements, including two-reflector etalon-like internal structures and three-mirror geometries relevant to coupled cavities, filter cavities, and membrane-in-the-middle architectures. These results are particularly relevant to precision interferometry

and related coupled-cavity quantum optical systems, in which engineered pole splittings and linewidths directly determine filtering, resonance hybridization, and quantum-noise shaping [22–26,33]. Extensions beyond the present 1D treatment include angular and transverse effects, such as walk-off losses in intracavity etalons [34].

Overall, the framework presented here bridges exact transfer-matrix methods with a mode-resolved non-Hermitian viewpoint. It provides practical tools for exact pole calculation, weak-reflector asymptotics, and numerical pole tracking, and offers a flexible basis for the analysis and design of advanced interferometric and optomechanical cavity systems.

Author Contributions: V.V. and N.K. conceived the project. V.V. carried out the calculations and simulations, with guidance from N.K. M.K. supervised the project. All authors contributed to the writing of the manuscript. All authors have read and agreed to the published version of the manuscript.

Funding: This research was supported by the University of Rijeka under the project uniri-mz-25-54 (QOMPFOQM), the Croatian Science Foundation under the project IP-2024-05-5670 (MIMIQ.ME) and the Ministry of Science, Education and Youth of the Republic of Croatia Grant No. PK.1.1.10.0002.

Institutional Review Board Statement: Not applicable.

Informed Consent Statement: Not applicable.

Data Availability Statement: No external datasets were used in this study. Numerical data generated for the figures and analyses are available from the corresponding author upon reasonable request.

Acknowledgments: During the preparation of this manuscript, the authors used OpenAI GPT-5.5 to improve clarity and grammar. The authors reviewed and edited the generated text and take full responsibility for the content of this publication.

Conflicts of Interest: The authors declare no conflicts of interest.

Appendix A. Equivalence of Transfer-Matrix and Scattering/Boundary-Condition Approaches

This appendix shows that the reduced denominator $\mathcal{D}(\omega)$ obtained from the transfer-matrix method (Section 3) is equivalent, up to a nonzero analytic prefactor, to the denominator obtained by a direct scattering/boundary-condition construction.

Appendix A.1. Reference Planes and Field Notation

We work at normal incidence with time dependence $e^{-i\omega t}$ and define $k = \omega/c$. We introduce two reference planes on the vacuum side of the slab interfaces (Figure A1):

- Plane a: vacuum side of the slab front face at $z = z_0$,
- Plane b: vacuum side of the slab back face at $z = z_0 + d$.

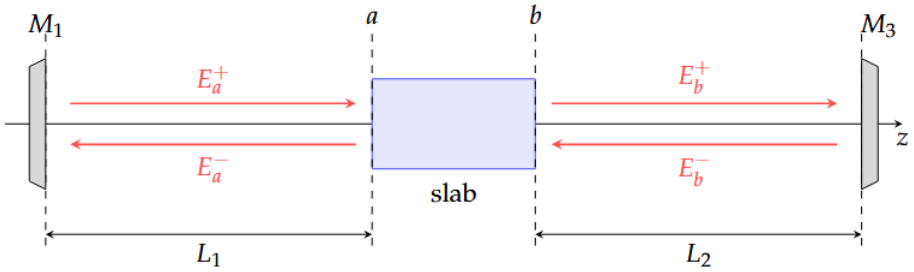


Figure A1. Reference planes a (front face) and b (back face) used in Appendix A, with forward/backward amplitudes $E^{\pm}_{a,b}$ and vacuum gaps $L_{1,2}$.

At each plane $j \in \{a, b\}$, we denote the forward and backward amplitudes by E_j^+ (right-going) and E_j^- (left-going), so that locally, in vacuum,

$$E(z) = E^+ e^{ikz} + E^- e^{-ikz}. \tag{A1}$$

The vacuum gaps are $L_1 = z_0$ between M_1 and plane a, and $L_2 = L - z_0 - d$ between plane b and M_3, as in the main text.

Appendix A.2. Mirror Boundary Conditions

Let E_{in} be the incident field from the left and E_{ref} the reflected field on the input side. Let $E_1^{\pm}$ denote the amplitudes just inside the cavity at mirror M_1, and $E_3^{\pm}$ denote the corresponding amplitudes just inside the cavity at mirror M_3. Using the transfer-matrix convention of the main text, the left mirror relation is

$$\begin{pmatrix} E_{\text{ref}} \\ E_{\text{in}} \end{pmatrix} = \mathbf{M}_1(\omega) \begin{pmatrix} E_1^- \\ E_1^+ \end{pmatrix} = \frac{1}{t_1(\omega)} \begin{pmatrix} 1 & r_1(\omega) \\ r_1(\omega) & 1 \end{pmatrix} \begin{pmatrix} E_1^- \\ E_1^+ \end{pmatrix}. \tag{A2}$$

The second row gives

$$E_{\text{in}} = \frac{r_1(\omega)\, E_1^- + E_1^+}{t_1(\omega)}, \tag{A3}$$

hence

$$E_1^+ = t_1(\omega)\, E_{\text{in}} - r_1(\omega)\, E_1^-. \tag{A4}$$

Propagation from M_1 to plane a gives

$$E_a^+ = E_1^+ e^{ikL_1}, \qquad E_a^- = E_1^- e^{-ikL_1}, \tag{A5}$$

or equivalently

$$E_1^+ = E_a^+ e^{-ikL_1}, \qquad E_1^- = E_a^- e^{ikL_1}. \tag{A6}$$

Substituting these into Equation (A4) gives

$$E_a^+ e^{-ikL_1} = t_1(\omega)\, E_{\text{in}} - r_1(\omega)\, E_a^- e^{ikL_1}, \tag{A7}$$

and therefore the left boundary condition at plane a is

$$E_a^+ = t_1(\omega)\, e^{ikL_1}\, E_{\text{in}} - r_1(\omega)\, e^{i2kL_1}\, E_a^-. \tag{A8}$$

On the right, let E_{out} be the transmitted field outside mirror M_3. There is no field incident from the right, so the external backward amplitude vanishes. Thus,

$$\begin{pmatrix} E_3^- \\ E_3^+ \end{pmatrix} = \mathbf{M}_3(\omega) \begin{pmatrix} 0 \\ E_{\text{out}} \end{pmatrix} = \frac{1}{t_3(\omega)} \begin{pmatrix} 1 & r_3(\omega) \\ r_3(\omega) & 1 \end{pmatrix} \begin{pmatrix} 0 \\ E_{\text{out}} \end{pmatrix}. \tag{A9}$$

This yields

$$E_3^- = \frac{r_3(\omega)}{t_3(\omega)} E_{\text{out}}, \qquad E_3^+ = \frac{1}{t_3(\omega)} E_{\text{out}}, \tag{A10}$$

so that

$$E_3^- = r_3(\omega)\, E_3^+. \tag{A11}$$

Propagation between plane b and M_3 gives

$$E_b^- = E_3^- e^{ikL_2}, \qquad E_b^+ = E_3^+ e^{-ikL_2}, \tag{A12}$$

or equivalently

$$E_3^- = E_b^-\, e^{-ikL_2}, \qquad E_3^+ = E_b^+\, e^{ikL_2}. \tag{A13}$$

Substituting into Equation (A11) gives

$$E_b^-\, e^{-ikL_2} = r_3(\omega)\, E_b^+\, e^{ikL_2}, \tag{A14}$$

hence the right boundary condition at plane b is

$$E_b^- = r_3(\omega)\, e^{i2kL_2}\, E_b^+. \tag{A15}$$

Appendix A.3. Slab Scattering

For a general two-port internal element, the scattering relations between planes a and b are

$$E_a^- = r_s^{(L)}(\omega)\, E_a^+ + t_s^{(R)}(\omega)\, E_b^-, \tag{A16}$$

$$E_b^+ = t_s^{(L)}(\omega)\, E_a^+ + r_s^{(R)}(\omega)\, E_b^-. \tag{A17}$$

Here $r_s^{(L)}$ and $r_s^{(R)}$ are the reflection amplitudes for incidence from the left and from the right, while $t_s^{(L)}$ and $t_s^{(R)}$ are the transmission amplitudes for left-to-right and right-to-left transmission.

For a reciprocal optical element, the scattering matrix is symmetric (for the same field normalization on both sides), which implies

$$t_s^{(L)}(\omega) = t_s^{(R)}(\omega). \tag{A18}$$

For the present case of a uniform slab embedded in the same medium (vacuum) on both sides, the structure is also left–right symmetric, so one further has

$$r_s^{(L)}(\omega) = r_s^{(R)}(\omega). \tag{A19}$$

We nevertheless keep the more general notation in the intermediate algebra and specialize only when identifying the transfer-matrix coefficients.

Using the right boundary condition (A15) to eliminate E_b^- from Equation (A17) gives

$$E_b^+ = t_s^{(L)}(\omega)\, E_a^+ + r_s^{(R)}(\omega)\, r_3(\omega) e^{i2kL_2}\, E_b^+, \tag{A20}$$

so that

$$E_b^+ = \frac{t_s^{(L)}(\omega)}{1 - r_s^{(R)}(\omega)\, r_3(\omega) e^{i2kL_2}}\, E_a^+. \tag{A21}$$

Then, Equation (A15) gives

$$E_b^- = \frac{t_s^{(L)}(\omega)\, r_3(\omega) e^{i2kL_2}}{1 - r_s^{(R)}(\omega)\, r_3(\omega) e^{i2kL_2}}\, E_a^+. \tag{A22}$$

Substituting this into Equation (A16) yields

$$E_a^- = \left[r_s^{(L)}(\omega) + \frac{t_s^{(L)}(\omega) t_s^{(R)}(\omega)\, r_3(\omega) e^{i2kL_2}}{1 - r_s^{(R)}(\omega)\, r_3(\omega) e^{i2kL_2}} \right] E_a^+. \tag{A23}$$

Finally, substituting Equation (A23) into the left boundary condition (A8) gives

$$E_a^+ = t_1(\omega)e^{ikL_1}E_{\text{in}} - r_1(\omega)e^{i2kL_1}\left[r_s^{(L)}(\omega) + \frac{t_s^{(L)}(\omega)t_s^{(R)}(\omega)\,r_3(\omega)e^{i2kL_2}}{1 - r_s^{(R)}(\omega)\,r_3(\omega)e^{i2kL_2}}\right]E_a^+. \tag{A24}$$

Rearranging gives

$$E_a^+ = \frac{t_1(\omega)e^{ikL_1}}{\mathcal{D}_{\text{sc}}(\omega)}\,E_{\text{in}}, \tag{A25}$$

where

$$\mathcal{D}_{\text{sc}}(\omega) = 1 + r_1(\omega)e^{i2kL_1}\left[r_s^{(L)}(\omega) + \frac{t_s^{(L)}(\omega)t_s^{(R)}(\omega)\,r_3(\omega)e^{i2kL_2}}{1 - r_s^{(R)}(\omega)\,r_3(\omega)e^{i2kL_2}}\right]. \tag{A26}$$

The pole frequencies $\tilde{\omega}_\mu$ are therefore determined by

$$\mathcal{D}_{\text{sc}}(\tilde{\omega}_\mu) = 0, \qquad \mathfrak{Im}\,\tilde{\omega}_\mu < 0. \tag{A27}$$

Appendix A.4. Identification with the Transfer-Matrix Denominator

To connect this result to the transfer-matrix formulation, write the slab block as

$$\mathbf{S}(\omega) = \begin{pmatrix} A_s(\omega) & B_s(\omega) \\ C_s(\omega) & D_s(\omega) \end{pmatrix}, \tag{A28}$$

with the transfer relation

$$\begin{pmatrix} E_a^- \\ E_a^+ \end{pmatrix} = \mathbf{S}(\omega)\begin{pmatrix} E_b^- \\ E_b^+ \end{pmatrix}. \tag{A29}$$

Explicitly,

$$E_a^- = A_s(\omega)\,E_b^- + B_s(\omega)\,E_b^+, \tag{A30}$$
$$E_a^+ = C_s(\omega)\,E_b^- + D_s(\omega)\,E_b^+. \tag{A31}$$

For incidence from the left only, $E_b^- = 0$, so

$$E_a^- = B_s(\omega)\,E_b^+, \qquad E_a^+ = D_s(\omega)\,E_b^+, \tag{A32}$$

and therefore

$$r_s^{(L)}(\omega) = \frac{E_a^-}{E_a^+} = \frac{B_s(\omega)}{D_s(\omega)}, \qquad t_s^{(L)}(\omega) = \frac{E_b^+}{E_a^+} = \frac{1}{D_s(\omega)}. \tag{A33}$$

For incidence from the right only, $E_a^+ = 0$, so

$$0 = C_s(\omega)\,E_b^- + D_s(\omega)\,E_b^+, \tag{A34}$$

hence

$$E_b^+ = -\frac{C_s(\omega)}{D_s(\omega)}\,E_b^-. \tag{A35}$$

This gives

$$r_s^{(R)}(\omega) = \frac{E_b^+}{E_b^-} = -\frac{C_s(\omega)}{D_s(\omega)}. \tag{A36}$$

Moreover,

$$E_a^- = A_s(\omega)\, E_b^- + B_s(\omega)\, E_b^+ = \left(A_s(\omega) - \frac{B_s(\omega) C_s(\omega)}{D_s(\omega)} \right) E_b^- . \tag{A37}$$

Using

$$A_s(\omega) D_s(\omega) - B_s(\omega) C_s(\omega) = 1, \tag{A38}$$

one obtains

$$E_a^- = \frac{1}{D_s(\omega)}\, E_b^- , \tag{A39}$$

and hence

$$t_s^{(R)}(\omega) = \frac{E_a^-}{E_b^-} = \frac{1}{D_s(\omega)}. \tag{A40}$$

Collecting these results,

$$t_s^{(L)}(\omega) = t_s^{(R)}(\omega) = \frac{1}{D_s(\omega)}, \qquad r_s^{(L)}(\omega) = \frac{B_s(\omega)}{D_s(\omega)}, \qquad r_s^{(R)}(\omega) = -\frac{C_s(\omega)}{D_s(\omega)}. \tag{A41}$$

For a symmetric slab embedded in vacuum, one has $B_s(\omega) = -C_s(\omega)$, so indeed

$$r_s^{(L)}(\omega) = r_s^{(R)}(\omega). \tag{A42}$$

Substituting Equation (A41) into Equation (A26) gives

$$\mathcal{D}_{\mathrm{sc}}(\omega) = 1 + r_1(\omega) e^{i2kL_1} \left[\frac{B_s(\omega)}{D_s(\omega)} + \frac{r_3(\omega) e^{i2kL_2}}{D_s(\omega)\left(D_s(\omega) + C_s(\omega) r_3(\omega) e^{i2kL_2}\right)} \right]. \tag{A43}$$

Combining the terms in brackets over the common denominator $D_s(\omega) + C_s(\omega) r_3(\omega) e^{i2kL_2}$,

$$\frac{B_s}{D_s} + \frac{r_3 e^{i2kL_2}}{D_s(D_s + C_s r_3 e^{i2kL_2})} = \frac{B_s(D_s + C_s r_3 e^{i2kL_2}) + r_3 e^{i2kL_2}}{D_s(D_s + C_s r_3 e^{i2kL_2})}. \tag{A44}$$

Using $A_s D_s - B_s C_s = 1$, the numerator becomes

$$B_s D_s + B_s C_s r_3 e^{i2kL_2} + r_3 e^{i2kL_2} = B_s D_s + A_s D_s\, r_3 e^{i2kL_2} = D_s\left(B_s + A_s r_3 e^{i2kL_2}\right), \tag{A45}$$

so

$$\mathcal{D}_{\mathrm{sc}}(\omega) = 1 + r_1(\omega) e^{i2kL_1} \frac{B_s(\omega) + A_s(\omega) r_3(\omega) e^{i2kL_2}}{D_s(\omega) + C_s(\omega) r_3(\omega) e^{i2kL_2}}. \tag{A46}$$

Bringing to a common denominator finally yields

$$\mathcal{D}_{\mathrm{sc}}(\omega) = \frac{D_s(\omega) + B_s(\omega)\, r_1(\omega) e^{i2kL_1} + C_s(\omega)\, r_3(\omega) e^{i2kL_2} + A_s(\omega)\, r_1(\omega) r_3(\omega) e^{i2k(L_1+L_2)}}{D_s(\omega) + C_s(\omega)\, r_3(\omega) e^{i2kL_2}}. \tag{A47}$$

The numerator is exactly the reduced denominator of Equation (23), $\mathcal{D}(\omega)$. Thus, $\mathcal{D}_{\mathrm{sc}}(\omega)$ and $\mathcal{D}(\omega)$ have the same zeros, provided that $D_s(\omega) + C_s(\omega) r_3(\omega) e^{i2kL_2}$ is finite and nonzero at the cavity poles. Therefore the scattering/boundary-condition construction yields the same pole condition as the TMM: the condition stated in Equation (A27) is equivalent to Equation (25).

Appendix B. Weak-Slab Expansion in the Thin-Element Limit

This appendix records the short algebraic step connecting the exact reduced denominator to the first-order weak-reflector form in the thin-element limit, where the internal slab is

approximated by an effective lumped reflector. All transfer-matrix and phase conventions are the same as in the main text.

Appendix B.1. Weak-Reflector Expansion of the Slab Block

For a sufficiently weak thin internal element, or equivalently for an effective lumped-reflector description, the internal transfer-matrix may be written as a perturbation of the identity,

$$\mathbf{S}(\omega) = \begin{pmatrix} A_s(\omega) & B_s(\omega) \\ C_s(\omega) & D_s(\omega) \end{pmatrix}, \tag{A48}$$

with

$$A_s(\omega) = 1 + \mathcal{O}(r_m^2), \tag{A49}$$
$$D_s(\omega) = 1 + \mathcal{O}(r_m^2), \tag{A50}$$
$$B_s(\omega) = r_m(\omega) + \mathcal{O}(r_m^2), \tag{A51}$$
$$C_s(\omega) = -r_m(\omega) + \mathcal{O}(r_m^2), \tag{A52}$$

where $r_m(\omega)$ is the effective amplitude reflectivity introduced in Equation (4). For a thin symmetric internal reflector this form is immediate. For a finite-thickness weak slab, the first-order correction should instead be obtained by expanding the exact slab matrix elements A_s, B_s, C_s, D_s directly, as noted in Section 4.2.

Appendix B.2. Expansion of the Exact Denominator

Starting from the exact reduced denominator,

$$\mathcal{D}(\omega) = D_s(\omega) + B_s(\omega)\, r_1(\omega)\, e^{i2kL_1} + C_s(\omega)\, r_3(\omega)\, e^{i2kL_2} + A_s(\omega)\, r_1(\omega) r_3(\omega)\, e^{i2k(L_1+L_2)}, \tag{A53}$$

and inserting Equations (A49)–(A52), one obtains to first order in r_m,

$$\mathcal{D}(\omega) = 1 + r_1(\omega) r_3(\omega) e^{i2k(L_1+L_2)} + r_m(\omega)\, r_1(\omega) e^{i2kL_1} - r_m(\omega)\, r_3(\omega) e^{i2kL_2} + \mathcal{O}(r_m^2). \tag{A54}$$

For the finite-thickness slab of Section 3, one has $L_1 = z_0$, $L_2 = L - z_0 - d$, and $L_1 + L_2 = L - d$. In the thin-element limit $d \to 0$ used here, this reduces to

$$L_1 = z_0, \qquad L_2 = L - z_0, \qquad L_1 + L_2 = L. \tag{A55}$$

Thus, the denominator becomes

$$\mathcal{D}(\omega, z_0) = \mathcal{D}_0(\omega) + \mathcal{D}_1(\omega, z_0) + \mathcal{O}(r_m^2), \tag{A56}$$

with

$$\mathcal{D}_0(\omega) = 1 + r_1(\omega)\, r_3(\omega)\, e^{i2kL}, \tag{A57}$$

and

$$\mathcal{D}_1(\omega, z_0) = r_m(\omega)\, r_1(\omega)\, e^{i2kz_0} - r_m(\omega)\, r_3(\omega)\, e^{i2k(L-z_0)}. \tag{A58}$$

Equation (A58) is the key ingredient needed to pass from the exact transfer-matrix denominator to the first-order weak-reflector form used in Section 4. The two terms in $\mathcal{D}_1$ are the two mirror-side first-order scattering contributions, and their interference is what produces the mode-dependent complex quantity $\zeta_\mu(z_0)$ introduced in Equation (38).

Appendix C. Limitations of the Weak-Reflector Model

The weak model does not always approximate the full TMM curves because it treats the slab as a localized, optically weak internal reflector and retains only the first-order scattering response. For a fixed cavity mode, taken here as $\mu = 0$, the main small parameter is the effective slab reflectivity

$$r_{m,0}(d) = \left.\frac{B_s(\omega)}{D_s(\omega)}\right|_{\omega=\tilde{\omega}_0^{(0)}}. \tag{A59}$$

For a lossless slab, this may be written as

$$r_{m,0}(d) = \frac{\mathrm{i}\beta_0 \sin\phi_0(d)}{\cos\phi_0(d) - i\alpha_0 \sin\phi_0(d)}, \tag{A60}$$

where

$$\phi_0(d) = n_s(\tilde{\omega}_0^{(0)})\, k_0 d, \qquad \alpha_0 = \frac{n_s^2(\tilde{\omega}_0^{(0)}) + 1}{2n_s(\tilde{\omega}_0^{(0)})}, \qquad \beta_0 = \frac{n_s^2(\tilde{\omega}_0^{(0)}) - 1}{2n_s(\tilde{\omega}_0^{(0)})}. \tag{A61}$$

The corresponding single-mode validity metric is

$$M_0(d) \equiv |r_{m,0}(d)|. \tag{A62}$$

The first-order ridge shift

$$\delta\omega_0(z_0) = -\frac{c}{2L}\, \mathfrak{Im}\, \zeta_0(z_0), \tag{A63}$$

with

$$\zeta_0(z_0) = r_{m,0}\left[\frac{e^{-i2k_0(L-z_0)}}{r_3} + r_3 e^{+i2k_0(L-z_0)}\right], \tag{A64}$$

is reliable only when

$$M_0(d) \ll 1. \tag{A65}$$

This condition can fail even for a lossless slab when the optical thickness approaches a quarter-wave-like condition,

$$nd \approx \frac{(2q+1)\lambda}{4}, \qquad q \in \mathbb{Z}, \tag{A66}$$

because then $|r_{m,0}|$ becomes large and multiple internal reflections, included in the full TMM but neglected at first order, shift the ridges in amplitude, phase, and sometimes baseline frequency. Conversely, $M_0(d)$ returns close to zero near half-wave slab conditions,

$$nd = q\frac{\lambda}{2}. \tag{A67}$$

Thus, for a single mode, increasing d does not make the weak-reflector condition permanently invalid; instead, the validity metric remains an oscillatory function of the slab phase.

In addition, the thin reflector interpretation used for the first-order ridge curves requires the slab to remain geometrically small compared with the cavity length,

$$\frac{d}{L} \ll 1, \tag{A68}$$

so that it can still be treated as a small internal element rather than as an extended part of the cavity. In the present calculations, $L = 42$ mm, so $d/L < 0.01$ corresponds to

$d < 420$ µm, while $d/L > 0.05$ corresponds to $d > 2.1$ mm, where the thin-effective-reflector interpretation becomes questionable.

Figure A2 shows that, for a single mode, the validity metric does not vary monotonically with thickness. Instead, it oscillates with the slab phase $\phi_0(d)$, with minima near half-wave slab conditions and maxima near quarter-wave-like conditions. For a nondispersive lossless slab, the wavelength dependence of $r_{m,0}(d)$ enters only through the optical phase $\phi_0 = 2\pi nd/\lambda$. For a dispersive or absorptive slab, however, $n_s(\omega)$ also changes the coefficients α_0 and β_0, so the wavelength affects both the oscillation phase and the amplitude of the effective reflectivity.

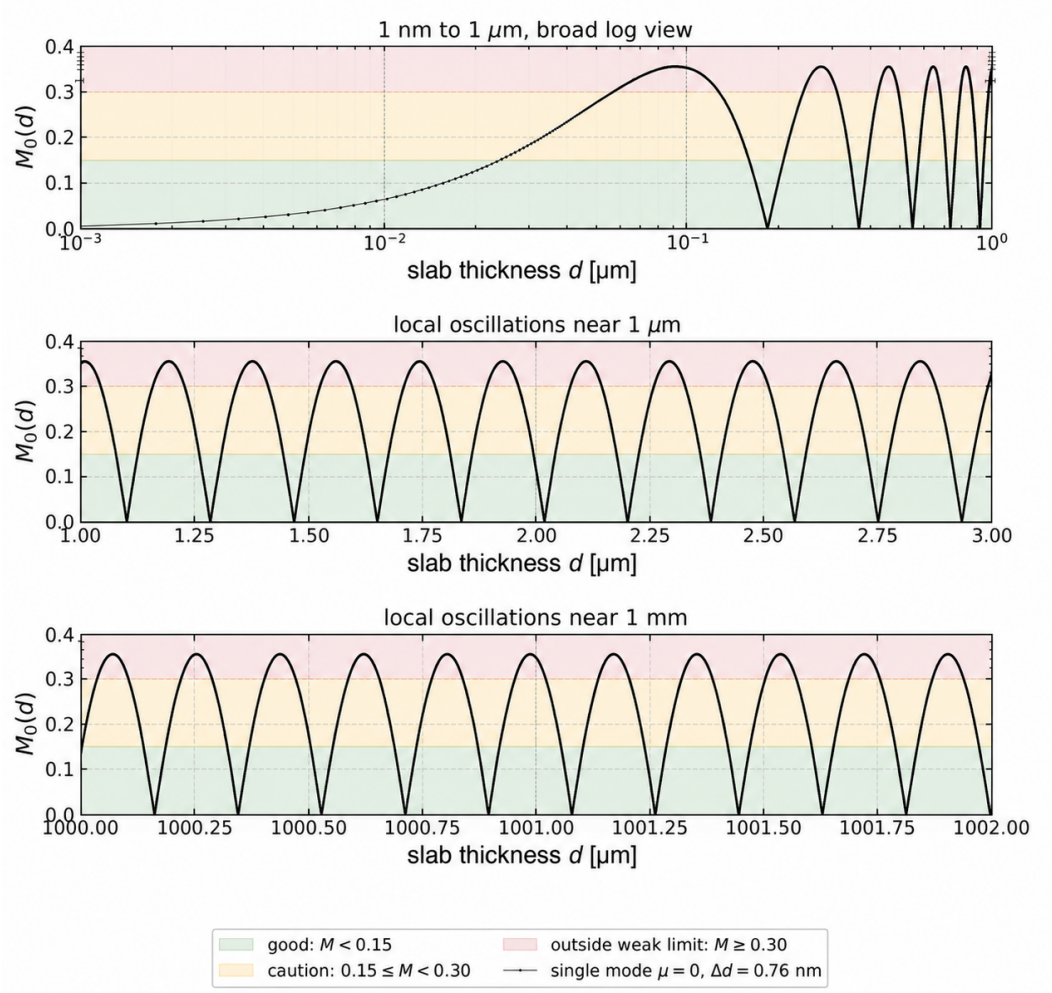


Figure A2. Single-mode validity range of the first-order weak-reflector model. The three panels show the effective slab reflectivity metric $M_0(d) = |r_{m,0}|$, with $r_{m,0} = B_s(\tilde{\omega}_0^{(0)})/D_s(\tilde{\omega}_0^{(0)})$ for distinct ranges of slab thickness. The slab thickness increment used in the simulation is 0.76 nm, with interpolation between resulting points. The broad logarithmic views show that the dense regions at larger thickness arise from rapid optical-thickness oscillations, while the local zooms show that the same oscillatory structure persists at both micrometer and millimeter thicknesses. The shaded regions indicate representative ranges where the first-order expansion is expected to be good, used with caution, or outside the weak-reflector limit.

The structural difference between the exact finite-slab response and the weak-reflector description can be seen by comparing their thickness derivatives. For a thickness sweep at fixed front-face position z_0, we have $L_1 = z_0$, $L_2 = L - z_0 - d$, so that

$$\partial_d L_1 = 0, \qquad \partial_d L_2 = -1, \qquad \partial_d (L_1 + L_2) = -1. \tag{A69}$$

Writing

$$\phi = n_s(\omega)kd, \qquad \alpha_s = \frac{n_s^2+1}{2n_s}, \qquad \beta_s = \frac{n_s^2-1}{2n_s}, \tag{A70}$$

direct differentiation of the exact reduced denominator gives

$$\begin{aligned}\partial_d \mathcal{D} = {} & n_s k[-\sin\phi - i\alpha_s \cos\phi] \\ & + r_1 e^{i2kz_0}[i\beta_s n_s k \cos\phi] \\ & + r_3 e^{i2k(L-z_0-d)}[-i\beta_s n_s k\cos\phi - 2k\beta_s \sin\phi] \\ & + r_1 r_3 e^{i2k(L-d)}[n_s k(-\sin\phi + i\alpha_s\cos\phi) - i2k(\cos\phi + i\alpha_s \sin\phi)].\end{aligned} \tag{A71}$$

Here, we write a first-order weak-reflector description in a simpler form,

$$r_m(\omega) \equiv \epsilon(\omega)\, e^{i\psi(\omega)} \tag{A72}$$

where $\epsilon(\omega) = |r_m(\omega)|$ is the reflection amplitude and $\psi(\omega) = \arg r_m(\omega)$ is its phase. Now the thickness dependence can be instead compressed into the effective complex reflectivity

$$r_m(d) = \epsilon(d) e^{i\psi(d)}, \tag{A73}$$

where, for notational simplicity, the explicit dependence on ω has been suppressed. Since

$$\partial_d r_m = e^{i\psi(d)}[\partial_d \epsilon(d) + i\epsilon(d)\,\partial_d \psi(d)], \tag{A74}$$

and

$$\mathcal{D}_1(\omega, z_0; d) = r_m(d) r_1(\omega) e^{i2kz_0} - r_m(d) r_3(\omega) e^{i2k(L-z_0)}, \tag{A75}$$

one obtains

$$\partial_d \mathcal{D}_1 = e^{i\psi(d)}[\partial_d \epsilon(d) + i\epsilon(d)\,\partial_d \psi(d)]\left[r_1(\omega)e^{i2kz_0} - r_3(\omega)e^{i2k(L-z_0)}\right]. \tag{A76}$$

Equation (A76) has a separable form: thickness only changes the effective amplitude and phase of $r_m(d)$, multiplying the same two-path interference factor as in the first-order correction. By contrast, Equation (A71) contains independent slab matrix and propagation phase terms, which is why the full transfer-matrix ridges can develop shifts and shape changes that are not reproduced by the first-order weak-reflector model.

Appendix D. Parameter Sensitivities of the Reduced Denominator

This appendix makes explicit how different swept parameters enter the pole condition. Let s denote any real control parameter, such as an internal position, internal reflectivity, slab thickness, or absorption. The poles satisfy

$$\mathcal{D}(\tilde{\omega}_\mu(s); s) = 0. \tag{A77}$$

Provided the pole is simple, implicit differentiation gives

$$\frac{d\tilde{\omega}_\mu}{ds} = -\left.\frac{\partial_s \mathcal{D}(\omega; s)}{\partial_\omega \mathcal{D}(\omega; s)}\right|_{\omega=\tilde{\omega}_\mu(s)}. \tag{A78}$$

The derivative ∂_s is taken at fixed ω, while ∂_ω includes the explicit frequency dependence of the propagation phases, mirror coefficients, and slab response.

Since the full transfer-matrix denominator $D(\omega; s)$ and the reduced denominator $\mathcal{D}(\omega; s)$ differ only by a nonzero analytic prefactor,

$$D(\omega; s) = P_{\text{pref}}(\omega; s)\, \mathcal{D}(\omega; s), \tag{A79}$$

either denominator gives the same pole sensitivity. At a pole, $\mathcal{D}(\tilde{\omega}_\mu; s) = 0$, so the derivatives of the prefactor drop out:

$$\left.\frac{\partial_s D}{\partial_\omega D}\right|_{\tilde{\omega}_\mu} = \left.\frac{\partial_s \mathcal{D}}{\partial_\omega \mathcal{D}}\right|_{\tilde{\omega}_\mu}. \tag{A80}$$

For the single-slab reduced denominator,

$$\mathcal{D}(\omega) = D_s + B_s r_1 e^{i2kL_1} + C_s r_3 e^{i2kL_2} + A_s r_1 r_3 e^{i2k(L_1+L_2)}, \tag{A81}$$

the derivative with respect to a general parameter s is

$$\begin{aligned}\partial_s \mathcal{D} = {} & \partial_s D_s + r_1 e^{i2kL_1}[\partial_s B_s + i2kB_s\, \partial_s L_1] \\ & + r_3 e^{i2kL_2}[\partial_s C_s + i2kC_s\, \partial_s L_2] \\ & + r_1 r_3 e^{i2k(L_1+L_2)}[\partial_s A_s + i2kA_s\, \partial_s (L_1 + L_2)],\end{aligned} \tag{A82}$$

assuming that the end-mirror coefficients are not directly varied. If the mirror reflectivities are also swept, the corresponding terms proportional to $\partial_s r_1$ or $\partial_s r_3$ must be added. The transmission coefficients t_1 and t_3 appear only in the nonzero prefactor relating D and $\mathcal{D}$ and therefore do not change the pole locations, provided this prefactor remains finite and nonzero.

For a slab-position sweep at fixed thickness, $L_1 = z_0$ and $L_2 = L - z_0 - d$, so that

$$\partial_{z_0} L_1 = 1, \qquad \partial_{z_0} L_2 = -1, \qquad \partial_{z_0}(L_1 + L_2) = 0. \tag{A83}$$

If the slab material and thickness are fixed, then $\partial_{z_0} A_s = \partial_{z_0} B_s = \partial_{z_0} C_s = \partial_{z_0} D_s = 0$, and Equation (A82) reduces to

$$\partial_{z_0} \mathcal{D} = i2k\left[B_s r_1 e^{i2kL_1} - C_s r_3 e^{i2kL_2}\right]. \tag{A84}$$

Thus, a position sweep moves the poles by changing the relative propagation phases of the two mirror-side contributions.

In the thin weak-reflector limit, the first-order correction is

$$\mathcal{D}_1(\omega, z_0) = r_m(\omega) r_1(\omega) e^{i2kz_0} - r_m(\omega) r_3(\omega) e^{i2k(L-z_0)}. \tag{A85}$$

Therefore,

$$\partial_{z_0} \mathcal{D}_1 = i2k\, r_m(\omega)\left[r_1(\omega) e^{i2kz_0} + r_3(\omega) e^{i2k(L-z_0)}\right]. \tag{A86}$$

A reflectivity sweep enters differently. For an amplitude reflectivity sweep at a fixed phase, $r_m = \epsilon e^{i\psi}$ (cf. Equation (A72)), one obtains

$$\partial_\epsilon \mathcal{D}_1 = e^{i\psi}\left[r_1(\omega) e^{i2kz_0} - r_3(\omega) e^{i2k(L-z_0)}\right]. \tag{A87}$$

Thus, changing ϵ changes the strength of the internal scattering contribution, whereas changing z_0 changes the relative phase between the two contributions.

https://doi.org/10.3390/photonics13080721

For a finite slab, a thickness or material sweep acts through the slab matrix elements. For any slab parameter $s \in \{d, n', n''\}$, Equation (A82) applies with the derivatives $\partial_s A_s$, $\partial_s B_s$, $\partial_s C_s$, and $\partial_s D_s$ computed from

$$\phi(\omega) = n_s(\omega)\frac{\omega d}{c}. \tag{A88}$$

For an absorption sweep with $n_s = n' + in''$ and fixed n',

$$\partial_{n''} A_s = i\,\partial_{n_s} A_s, \qquad \partial_{n''} B_s = i\,\partial_{n_s} B_s, \tag{A89}$$

and similarly for C_s and D_s, provided the slab response is regarded as an analytic function of n_s. Such a sweep typically moves the relevant poles deeper into the lower half-plane, corresponding to an increase of $-2\,\mathfrak{Im}\,\tilde{\omega}_\mu$ and hence linewidth broadening.

For the three-mirror denominator,

$$\mathcal{D}_{3\mathrm{m}}(\omega) = 1 + r_1 r_2 e^{i2kL_1} + r_2 r_3 e^{i2kL_2} + r_1 r_3 e^{i2k(L_1+L_2)}, \tag{A90}$$

a sweep of the middle-mirror reflectivity gives

$$\partial_{r_2}\mathcal{D}_{3\mathrm{m}} = r_1 e^{i2kL_1} + r_3 e^{i2kL_2}. \tag{A91}$$

By contrast, translating the middle mirror at fixed total length, with

$$L_1 \mapsto L_1 + \Delta z, \qquad L_2 \mapsto L_2 - \Delta z, \tag{A92}$$

gives

$$\partial_{\Delta z}\mathcal{D}_{3\mathrm{m}} = i2k\,r_2\left[r_1 e^{i2kL_1} - r_3 e^{i2kL_2}\right]. \tag{A93}$$

Thus the middle-mirror reflectivity controls the coupling strength between the two subcavities, while its position controls their relative phase.

All sensitivity formulas above assume a simple pole, i.e.,

$$\partial_\omega \mathcal{D}(\tilde{\omega}_\mu(s); s) \neq 0. \tag{A94}$$

This is the scalar pole equation analogue of first-order perturbation theory for a simple isolated eigenvalue [35]. At degenerate poles, and in particular at exceptional points where non-Hermitian eigenvalues and eigenvectors coalesce, this simple-pole condition fails and a higher-order local expansion of $\mathcal{D}$ is required [36].

References

1. Bhawalkar, D.D. Effect of an internal Fabry–Pérot etalon on the modes of a resonator. *Opt. Commun.* **1977**, *23*, 427–429. [CrossRef]
2. Bernabeu, E.; Amaré, J.C.; Alvarez, J.M.; Moreno, F. Intensity transmitted by a Fabry–Perot etalon with another internal Fabry–Perot interferometer. *Appl. Opt.* **1981**, *20*, 2117–2120. [CrossRef] [PubMed]
3. Harris, S.J.; Weiner, A.M. Continuous wave intracavity dye laser spectroscopy. II. A parametric study. *J. Chem. Phys.* **1981**, *74*, 3673–3679. [CrossRef]
4. Kasper, J.V.; Pollock, C.R.; Curl, R.F.; Tittel, F.K. Computer control of broadly tunable lasers for high-resolution spectroscopy. *Appl. Opt.* **1982**, *21*, 236–247. [CrossRef] [PubMed]
5. Skeldon, M.D.; Bui, S.T. Temporal mode structure of a regenerative amplifier with intracavity étalons. *J. Opt. Soc. Am. B* **1993**, *10*, 677–683. [CrossRef]
6. Atherton, P.D. Tunable Fabry–Perot filters. *Opt. Eng.* **1981**, *20*, 805–814. [CrossRef]
7. Stevens, P.; Loriette, V.; Andia, M.; Glotin, F.; Lartaux-Vollard, A.; Leroy, N.; van de Walle, A. Resonant behavior and stability of a linear three-mirror cavity. *Class. Quantum Gravity* **2025**, *42*, 065014. [CrossRef]

8. Burmeister, O.; Bunkowski, A.; Schnabel, R.; Danzmann, K. All-reflective coupling of two optical cavities with 3-port gratings. *Opt. Express* **2010**, *18*, 9119–9132. [CrossRef] [PubMed]
9. Jayich, A.M.; Sankey, J.C.; Zwickl, B.M.; Yang, C.; Thompson, J.D.; Girvin, S.M.; Clerk, A.A.; Marquardt, F.; Harris, J.G.E. Dispersive optomechanics: A membrane inside a cavity. *New J. Phys.* **2008**, *10*, 095008. [CrossRef]
10. Thompson, J.D.; Zwickl, B.M.; Jayich, A.M.; Marquardt, F.; Girvin, S.M.; Harris, J.G.E. Strong dispersive coupling of a high-finesse cavity to a micromechanical membrane. *Nature* **2008**, *452*, 72–75. [CrossRef] [PubMed]
11. Aspelmeyer, M.; Kippenberg, T.J.; Marquardt, F. Cavity optomechanics. *Rev. Mod. Phys.* **2014**, *86*, 1391–1452. [CrossRef]
12. Haakestad, M.W.; Lamour, T.P.; Leindecker, N.; Marandi, A.; Vodopyanov, K.L. Intracavity trace molecular detection with a broadband mid-IR frequency comb source. *J. Opt. Soc. Am. B* **2013**, *30*, 631–640. [CrossRef]
13. Dumont, V.; Bernard, S.; Reinhardt, C.; Kato, A.; Ruf, M.; Sankey, J.C. Flexure-tuned membrane-at-the-edge optomechanical system. *Opt. Express* **2019**, *27*, 25731–25748. [CrossRef] [PubMed]
14. Bunkowski, A.; Burmeister, O.; Danzmann, K.; Schnabel, R. Input–output relations for a three-port grating coupled Fabry–Perot cavity. *Opt. Lett.* **2005**, *30*, 1183–1185. [CrossRef] [PubMed]
15. Nair, B.; Xuereb, A.; Dantan, A. Cavity optomechanics with arrays of thick dielectric membranes. *Phys. Rev. A* **2016**, *94*, 053812. [CrossRef]
16. Wei, X.; Yu, H.; Yang, C.; Li, Y. Controllable two-membrane-in-the-middle cavity optomechanical system. *Phys. Rev. A* **2019**, *99*, 023851. [CrossRef]
17. Piergentili, P.; Catalini, L.; Bawaj, M.; Zippilli, S.; Malossi, N.; Natali, R.; Vitali, D.; Di Giuseppe, G. Two-membrane cavity optomechanics. *New J. Phys.* **2018**, *20*, 083024. [CrossRef]
18. Marzioni, F.; Natali, R.; Malossi, N.; Vitali, D.; Di Giuseppe, G.; Piergentili, P. Two-membrane etalon. *Phys. Rev. A* **2025**, *111*, 013525. [CrossRef]
19. Hild, S.; Freise, A.; Mantovani, M.; Chelkowski, S.; Degallaix, J.; Schilling, R. Using the etalon effect for in-situ balancing of the Advanced Virgo arm cavities. *Class. Quantum Gravity* **2008**, *26*, 025005. [CrossRef]
20. Beausoleil, R.G.; Gustafson, E.K.; Fejer, M.M.; D'Ambrosio, E.; Kells, W.; Camp, J. Model of thermal wave-front distortion in interferometric gravitational-wave detectors. I. Thermal focusing. *J. Opt. Soc. Am. B* **2003**, *20*, 1247–1268. [CrossRef]
21. Zhao, C.; Degallaix, J.; Ju, L.; Fan, Y.; Blair, D.G.; Slagmolen, B.J.J.; Gray, M.B.; Mow-Lowry, C.M.; McClelland, D.E.; Hosken, D.J.; et al. Compensation of strong thermal lensing in high optical power cavities. *Phys. Rev. Lett.* **2006**, *96*, 231101. [CrossRef] [PubMed]
22. Evans, M.; Barsotti, L.; Fritschel, P.; Ganapathy, D.; Miao, H. Realistic filter cavities for advanced gravitational-wave detectors. *Phys. Rev. D* **2013**, *88*, 022002. [CrossRef]
23. A+ LIGO Detector Collaboration. Broadband quantum enhancement of the LIGO detectors with a 300-m filter cavity. *Phys. Rev. X* **2023**, *13*, 041021. [CrossRef]
24. Nishino, Y.; Danilishin, S.; Enomoto, Y.; Zhang, T. Frequency-dependent squeezing for gravitational-wave detection through quantum teleportation. *Phys. Rev. A* **2024**, *110*, 022601. [CrossRef]
25. Ding, J.; Capocasa, E.; Ahrend, I.; Liu, F.; Zhao, Y.; Barsuglia, M. Performance of multiple filter-cavity schemes for frequency-dependent squeezing in gravitational-wave detectors. *Phys. Rev. D* **2025**, *112*, 122001. [CrossRef]
26. Korobko, M. Quantum technologies for the Einstein Telescope. *Galaxies* **2025**, *13*, 11. [CrossRef]
27. Yeh, P. *Optical Waves in Layered Media*; John Wiley & Sons: New York, NY, USA, 1988; ISBN 0-471-82866-1.
28. Doost, M.B.; Langbein, W.W.; Muljarov, E.A. Resonant-state expansion applied to planar open optical systems. *Phys. Rev. A* **2012**, *85*, 023835. [CrossRef]
29. Kristensen, P.T.; Hughes, S. Modes and mode volumes of leaky optical cavities and plasmonic nanoresonators. *ACS Photonics* **2014**, *1*, 2–10. [CrossRef]
30. Ismail, N.; Kores, C.C.; Geskus, D.; Pollnau, M. Fabry–Pérot resonator: Spectral line shapes, generic and related Airy distributions, linewidths, finesses, and performance at low or frequency-dependent reflectivity. *Opt. Express* **2016**, *24*, 16366–16389. [CrossRef] [PubMed]
31. Vujnović, V.; Kralj, N.; Karuza, M. Detection of a semitransparent object with no exchange of quanta. *Opt. Express* **2025**, *33*, 1385–1393. [CrossRef] [PubMed]
32. Stevens, P.; Bonningues, P.-E.; Lesieur, T.; Glotin, F.; Loriette, V.; Andia, M.; Lartaux-Vollard, A.; Leroy, N.; van de Walle, A. Observation of resonant doublet and variable finesse in a tabletop meter-scale linear three-mirror cavity. *arXiv* **2025**, arXiv:2505.03416.
33. Junker, J.; Qin, J.; Adya, V.B.; Kijbunchoo, N.; Chua, S.S.Y.; McRae, T.G.; Slagmolen, B.J.J.; McClelland, D.E. Squeezing at the normal-mode splitting frequency of a nonlinear coupled cavity. *Phys. Rev. Lett.* **2025**, *134*, 243603. [CrossRef] [PubMed]
34. Eismann, U. Fabry–Pérot etalon walk-off loss in ring cavities. *Opt. Commun.* **2025**, *596*, 132381. [CrossRef]

35. Kato, T. *Perturbation Theory for Linear Operators*; Classics in Mathematics; Springer: Berlin/Heidelberg, Germany, 1995.
36. Miri, M.-A.; Alù, A. Exceptional points in optics and photonics. *Science* **2019**, *363*, eaar7709. [CrossRef] [PubMed]

Disclaimer/Publisher's Note: The statements, opinions and data contained in all publications are solely those of the individual author(s) and contributor(s) and not of MDPI and/or the editor(s). MDPI and/or the editor(s) disclaim responsibility for any injury to people or property resulting from any ideas, methods, instructions or products referred to in the content.